Award Number 07HQGR0042 and 06HQGR0109

ATTENUATION IN THE ATLANTIC COASTAL PLAIN OF VIRGINIA AND CENOZOIC FAULTING IMAGED IN THE EPICENTRAL AREA OF THE 1886 CHARLESTON, SOUTH CAROLINA EARTHQUAKE, USING DATA FROM SEISMIC REFLECTION PROFILES

Final Report
December 31, 2007

Martin C. Chapman
Telephone: (540) 231-5036
fax: (540) 231-3386
Email: mcc@vt.edu

Jacob N. Beale
Telephone: (540) 231-5036
Email: jbeale@vt.edu

John A. Hole
Telephone: (540) 231-3858
Email: jhole@vt.edu

Department of Geosciences
4044 Derring Hall
Virginia Polytechnic Institute and State University
Blacksburg, Virginia, 24061-0420

Research supported by the U.S. Geological Survey (USGS), Department of the Interior, under USGS award numbers 06HQGR0109 and 07HQGR0042. The views and conclusions contained in this document are those of the authors and should not be interpreted as necessarily representing the official policies, either expressed or implied, of the U.S. Government.

ATTENUATION IN THE ATLANTIC COASTAL PLAIN OF VIRGINIA AND CENOZOIC FAULTING IMAGED IN THE EPICENTRAL AREA OF THE 1886 CHARLESTON, SOUTH CAROLINA EARTHQUAKE, USING DATA FROM SEISMIC REFLECTION PROFILES

Martin C. Chapman, Jacob N. Beale and John A. Hole
Department of Geosciences
4044 Derring Hall
Virginia Polytechnic Institute and State University
Blacksburg, Virginia, 24061-0420

Telephone: (540) 231-5036 (mcc)
fax: (540) 231-3386
Email: mcc@vt.edu, jabeale@vt.edu, hole@vt.edu

ABSTRACT

The study is comprised of two parts. The first part quantifies attenuation of seismic waves in the Atlantic Coastal Plain. The second part presents the discovery of significant faulting at the epicenter of the 1886, Charleston, South Carolina earthquake.

The seismic quality factor Q for P-waves in Atlantic Coastal Plain sediments was estimated using data from the 2004 U.S. Geological Survey seismic survey on the eastern shore of Virginia. The estimates are based on spectral ratios derived from reflections and sediment-guided P-waves in Late Cretaceous and Tertiary sediments within the annular trough of the Late Eocene Chesapeake Bay impact structure. The estimates of Q for the frequency range 10 to 150 Hz are from 75 to 100, with the best estimate of 80 based on multi-channel stacking of spectral ratios from receivers in the offset range 200 to 2000 meters. This result is approximately a factor of two larger than results previously reported for the Charleston, South Carolina area, and is approximately one-half that recently reported for the Mississippi Embayment.

Seismic reflection line VT-3b collected in 1981 by the Virginia Tech Regional Geophysics Laboratory, in collaboration with the U.S. Geological Survey, along the Ashley River southeast of Summerville, South Carolina was reprocessed to investigate events exhibiting abnormal moveout. Processing included improved static correction, deconvolution and velocity analysis, giving an improved image of the shallow crust in the epicentral area of the 1886 shock. The result is a clearly imaged, down-to-the-east, steeply-dipping normal fault with approximately 200 m of vertical offset, displacing horizontally layered Lower Mesozoic sedimentary and volcanic rocks. The overlying Cretaceous and Tertiary sedimentary section, resolved by the data to within 100 meters of the ground surface, shows associated reverse displacement. Two other faults with substantial normal offset of Lower Mesozoic units were imaged immediately to the northwest of the major fault. This zone of faulting coincides exactly with the location of modern seismic activity, and maximum intensity mapped in 1886. We conclude that these faults are active and responsible for the Charleston earthquake.

Forward

The work described here was supported under two awards: numbers 06HQGR0109 and 07HQGR0042. The report is comprised of two parts because the subject material is distinct. The first part quantifies attenuation of seismic waves in the Atlantic Coastal Plain. The second part presents the discovery of significant faulting at the epicenter of the 1886, Charleston, South Carolina earthquake.

Part 1
Attenuation in the Atlantic Coastal Plain of Virginia
Grant Awards
06HQGR0109 & 07HQGR0042

Introduction

An important element in the prediction of strong ground-motion at sites on thick deposits of sediment is the value of Q at infinitesimal strain levels. Strains at depth in thick deposits are less than near the ground surface because of increased velocity and confining pressure. However, weak-motion estimates of Q are of relevance to strong-motion prediction in these cases because much attenuation of high-frequency energy can occur with relatively small strain at depth due to the large traveltime through the attenuating medium if Q is small (e.g., less than 50). In addition, the values of Q at small strains are a constraint for laboratory determinations of damping at higher strain levels.

Many previous studies report Q (for P and/or S-waves) of approximately 50 or less for sediments. For example, Boore et al. (2003) report Q for shear-waves (Q_s) typically in the range 25 to 36 (damping 0.020 to 0.014) at depths less than 100 meters for sites in California underlain by fine-grained material. It is not clear that Q increases markedly with depth in sediments. Abercrombie (1997) listed several studies in California using borehole data that indicate Q for P-waves (Q_p) less than 45 and Q_s less than 40 at depths greater than 100m. Abercrombie (1997) used a vertical array in the Cajon Pass borehole to determine Q_p and Q_s from spectral ratios at various depths, with data recorded from nearby earthquakes. A 300-m thick sedimentary section with P and S velocities of 1.79 and 0.657 km/s, respectively, exhibited $Q_s = 15$ and $Q_p = 26$.

Chapman et al. (2003) examined the attenuation of P and S-waves in the thick sediments of the Atlantic Coastal Plain near Charleston, South Carolina, using microearthquake spectral data from a network of stations in a joint inversion for the attenuation parameter kappa (κ). The results of that study indicated $\kappa = 0.035$ for transmission through 775 m of sediments with average S-wave velocity 700 m/s. This yields an average, whole-path Q_s of 32, for the sedimentary section in that study area. That estimate is consistent with the results cited above from California, and also with results by Liu et al. (1994) from similar work in the Mississippi Embayment. The estimate of Q_p reported by Chapman et al. (2003) for the Charleston, South Carolina area is 36.

Langston (2003a, 2003b) presented an assessment of potential bias in estimates of Q derived using the spectral ratio method. In principle, such bias could apply to many of the results mentioned above. The potential for this bias arises due to amplification of P and S-waves in very low-velocity material near the surface, which may mask the effect of intrinsic attenuation. Langston et al. (2005) report values of $Q_p = 200$ and $Q_s = 100$ for

the sediments of the Mississippi Embayment, derived from the spectral amplitude decay with distance of explosion-generated P-waves trapped within the sediment section, and the amplitude-distance attenuation of Rayleigh waves. Those estimates are in some cases more than a factor of 4 larger than earlier estimates reported for sedimentary environments, and have major implications for strong-motion prediction.

The purpose of this study is to determine a well-constrained, unbiased estimate of Q_p in the thick sediments of the Atlantic Coastal Plain, using high-frequency data from a seismic reflection/refraction survey conducted by the U.S. Geological Survey in eastern Virginia during 2004. The Atlantic Coastal Plain is the site of the major 1886 Charleston, South Carolina earthquake. The New Madrid Seismic Zone is located at the northern end of the synclinal Mississippi Embayment of the Gulf Coastal Plain, and the sediments found throughout the Coastal Plain region of the southern and southeastern United States have similar material properties.

The 2004 Chesapeake Bay Seismic Survey

The seismic survey was conducted by the U.S. Geological Survey on the Eastern Shore of Virginia (Figure 1.1). The 30 km profile was oriented along the radius of the 85 km wide, Late Eocene Chesapeake Bay impact structure (see Horton et al., 2005 for a summary and overview of studies of this feature). The survey involved 29 explosive sources with 1 km spacing and charge weights in the range 5 to 45 kg. The 602 receiver stations used 4.5 Hz vertical-component geophones, recorded at 500 samples/s with Refraction Technology, Inc. "Texan" digital acquisition units.

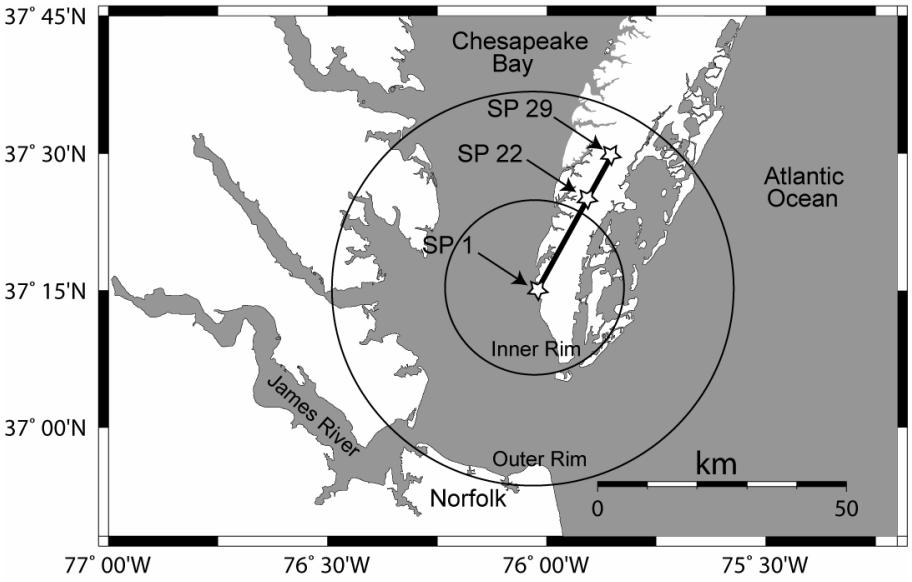

Figure 1.1 Map of the southeastern Virginia Coastal Plain area showing the location of the U.S. Geological Survey 2004 seismic survey (straight line). Stars show the locations of shotpoints 1, 22 and 29. The approximate locations of the rim of the inner crater and outer rim of the annular trough of the Chesapeake Bay impact structure are shown as the circles. The present study uses receivers located outside of the inner crater rim, recording data from shotpoints 22-29 on the northeastern end of the profile.

The data chosen for this study were collected on the northeastern end of the survey, and involve source and receiver pairs with raypaths that lie outside the 30-38 km wide excavation of the crystalline basement that is referred to variously as the "inner crater", "inner basin" or "central crater". Surrounding the inner crater is a flat-floored annular trough approximately 24 km in width. The outer margin or "outer rim" of this annular trough is generally considered to be the edge of the impact crater. Figure 1.1 shows the approximate location of the rim of the inner crater and the outer rim of the annular trough. All the data used for this study have raypaths confined to the annular trough. Crystalline basement within the annular trough is faulted, but is largely intact, not having been excavated as within the inner crater. The trough contains impact-disrupted sediments of Cretaceous to Lower Tertiary age that have been divided into crater units A and B and the Exmore beds (Gohn et al., 2005). Crater units A and B are mostly Cretaceous clastic sediments that were faulted, fractured and locally fluidized during the impact and shortly thereafter. The Exmore beds overlie units A and B and are interpreted as ocean-resurge sediments deposited by debris flows following impact (Gohn et al., 2005). Together, these impact-disrupted and impact-deposited sediments (units A, B and Exmore beds) will be referred to below as "syn-impact" sediments. Late Eocene to Quaternary post-impact sediments buried the crater and syn-impact deposits. Drill cores, a sonic log and a high-resolution seismic reflection profile in the western part of the annular trough at the NASA Langley Research Center in Hampton, Virginia show that the post-impact deposits are primarily marine deposits with largely horizontal continuous reflections. Some disturbed zones are present in the post-impact deposits, but are much less common than in the underlying syn-impact deposits (Powars et al., 2005; Catchings et al., 2005).

Velocity Model

Figure 1.2 shows the first-arrival, traveltime-distance data from shotpoints 22 and 23 to 4300 m offset. The traveltime-distance data suggest a two-layer over half-space model as a first approximation to the velocity structure within the study area on the northeastern end of the profile. We interpret the velocity increase from 1.6 km/s to 2.1 km/s to mark the transition from generally low-velocity post-impact sediments to syn-impact deposits, on the basis of similarities with the core and sonic log obtained at Hampton, Virginia (Catchings et al., 2005). The velocity increase from 2.1 to 5.3 km/s is interpreted as the transition from syn-impact sediments to crystalline basement. The resulting velocity model used for attenuation analysis is shown in Figure 1.3. It is a slightly more complex development of the two-layer structure implied by Figure 1.2, and is based on arrival-time modeling using synthetic seismograms. A 10 m thick, near-surface, low-velocity zone is added to the two-layer model inferred from the first-arrival traveltime data to model surface waves at near offsets. Slight velocity gradients, inferred on the basis of the sonic log from the Langley Research Center core hole and comparisons with synthetics, have been incorporated in each of the two layers inferred to represent post-impact and syn-impact deposits. The inferred post-impact sediments are modeled as 379 m thick. The underlying syn-impact sediments are modeled as 762 m in thickness, giving a depth to crystalline basement of 1.1 km. The velocity increase at a depth of 2.1 km has been added to the basement to match arrival-times of refracted arrivals at large offsets. Shear-wave velocities in the syn-impact sediments are based on an assumed P to S-wave velocity

ratio of 3.0, observed in the Coastal Plain sediments near Charleston, South Carolina (Chapman et al., 2003). The P-to-S velocity ratios for the post-impact sediments and near-surface low-velocity zone are 3.9 and 5.2, respectively, based on forward-modeling of Rayleigh waves.

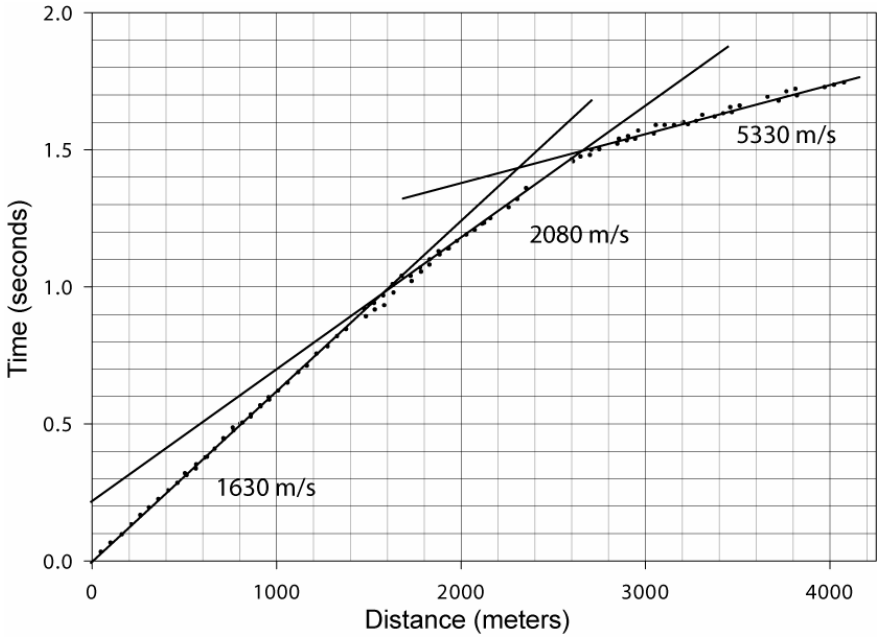

Figure 1.2 First-arrival traveltime-distance data from receivers on the northeastern end of the seismic survey, from shotpoints 22 and 23. The velocity structure for offsets in the range 0 to 4000 m can be approximated by 2 layers with P-wave velocities of 1630 and 2080 m/s, overlying a half-space with velocity 5330 m/s.

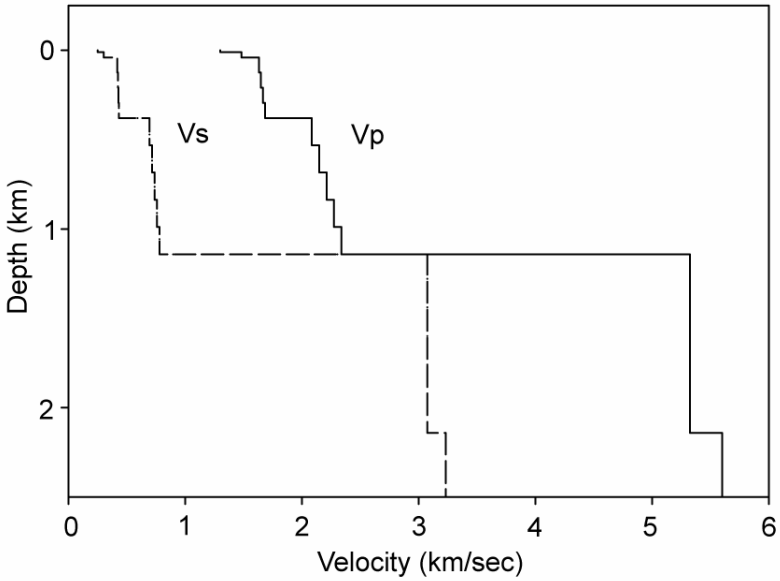

Figure 1.3. Velocity model used for analysis of data in this study.

Analysis Method

We assume a horizontally-layered velocity structure with frequency-independent Q, identical in all layers. Consider two windowed segments of a vertical-component reflection seismogram recorded at small source-receiver offset as shown in Figure 1.4. Each segment consists of N sample points with sample interval $\Delta\tau$. Assume that the early segment begins at two-way time τ_p, and that the later segment begins at time τ_q. For $N\Delta\tau$ sufficiently small, we can approximate the Fourier amplitude spectra $|Y_p(\omega)|$ and $|Y_q(\omega)|$ of the respective segments by assuming average values for the two-way traveltime for each segment. We express the ratio of the two amplitude spectra in Equation 1, where we have factored the terms involving Q from the summations, consistent with our assumption of small segment lengths.

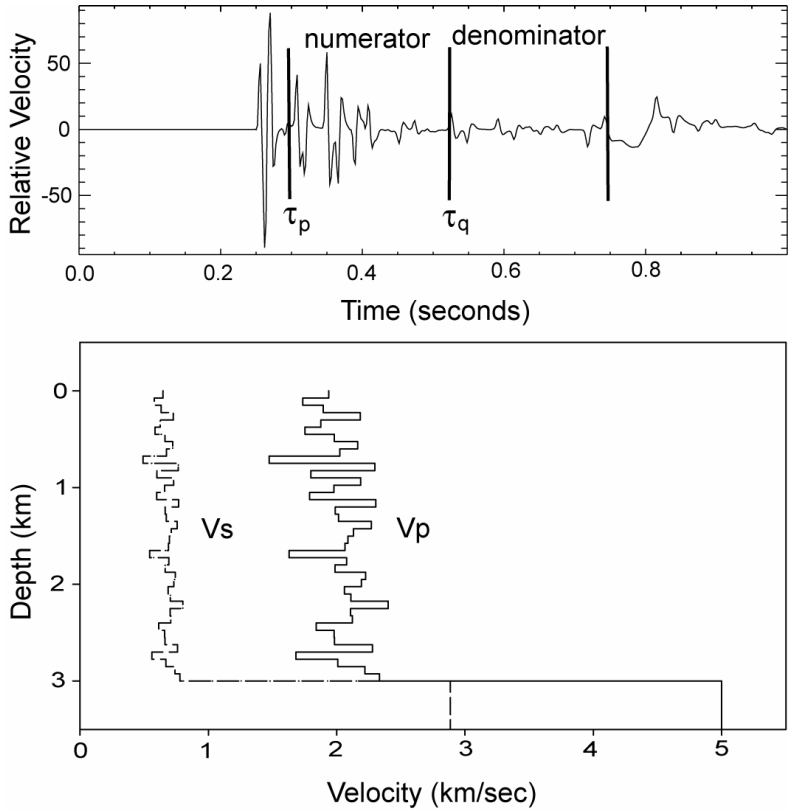

Figure 1.4. Example of the method used in this study to estimate Q from seismic reflection data. Top: Synthetic vertical-component velocity time series derived from a full- wavefield, frequency-wavenumber integration, for 500 meter source-receiver offset. An explosion source at 10 meter depth is assumed. The vertical lines indicate the time segments used to form the numerator and denominator spectra (τ_p and τ_q are the start times of the two windows). The end of the denominator segment coincides with the arrival of the Rayleigh wave. Bottom: hypothetical velocity structure assumed for the example. Density above 3 km depth is 2000 kg/m^3, and Q for both P and S-waves is 80.

$$\frac{|Y_p(\omega)|}{|Y_q(w)|} = \frac{\left|\left\{\sum_{j=p}^{p+N} \frac{\alpha_j}{v_j \tau_j} \exp(i\omega\tau_j)\right\}\right| \exp[-\omega(\tau_p + N\Delta\tau/2)/2Q]}{\left|\left\{\sum_{j=q}^{q+N} \frac{\alpha_j}{v_j \tau_j} \exp(i\omega\tau_j)\right\}\right| \exp[-\omega(\tau_q + N\Delta\tau/2)/2Q]} \qquad (1)$$

Each α_j in Equation 1 represents a product of transmission and reflection coefficients. Geometrical spreading is accounted for by $1/v_j\tau_j$, were v_j is the RMS velocity for the j'th reflection and τ_j is the two-way traveltime. All source and receiver effects are common for the two segments and thus do not appear in the spectral ratio. This eliminates a potential source of error described by Langston (2003a and 2003b). We assume that the amplitude spectra involving the two summations represent samples of random (Gaussian) processes, with expected values that are independent of frequency. Hence, the expected value of the ratio of the two terms involving summations is also frequency independent. The expected value of the logarithm of the spectral ratio is then

$$Ln\frac{|Y_p(\omega)|}{|Y_q(\omega)|} = C + (\tau_q - \tau_p)\omega/2Q, \qquad (2)$$

where C is a constant. Under these assumptions, estimation of Q amounts to determining the slope of a linear relationship between the expected value of the log-amplitude ratio and frequency. Note that the estimate of Q is independent of geometrical spreading. The ability to resolve the effect of attenuation depends not only on the value of Q, but also on the time separation (τ_q-τ_p) of the two windows used to calculate the spectral ratio, and the signal bandwidth.

Demonstration Using Synthetic Seismograms

The method is demonstrated using a full-wavefield synthetic seismogram computed using the frequency-wavenumber integration method (Herrmann, 2002). Figure 1.4 shows the synthetic vertical-component reflection seismogram and the corresponding velocity model. The source is an explosion at 10 m depth, and the source-receiver offset is 500 m. The velocity model is a rough approximation to that described above for the deeper part of the sedimentary sequence in the study area. This is modeled with a series of layers with constant thickness and random velocity fluctuations generated by adding a normally-distributed random value with zero mean and standard deviation of 200 m/s for P and 66 m/s for S to the constant mean value of 2.0 and 0.66 km/s for P and S- waves, respectively. The basement is modeled by a half-space with an increase in velocity to 5.5 and 2.8 km/s for P and S at a depth of 3.0 km. A value of 80 is used for Q in all layers, for both P and S-waves, and the source-time function is a parabolic pulse with duration 4 times the sample interval (0.002 s).

Figure 1.5 shows the amplitude spectra of the two time segments of the synthetic seismogram that form the numerator and dominator of the spectral ratio in Equation 2, along with the natural logarithm of the ratio. The latter shows a linear increase with frequency, as predicted. In the example, the lapse time separating the two windows (τ_q-τ_p) is only 0.225 seconds but the assumed value of Q = 80 is easily resolved from the slope of the log-spectral ratio versus frequency function. In this case, the bandwidth of

the data is 250 Hz: with real data, the usable bandwidth may be limited due to finite signal-to-noise ratio.

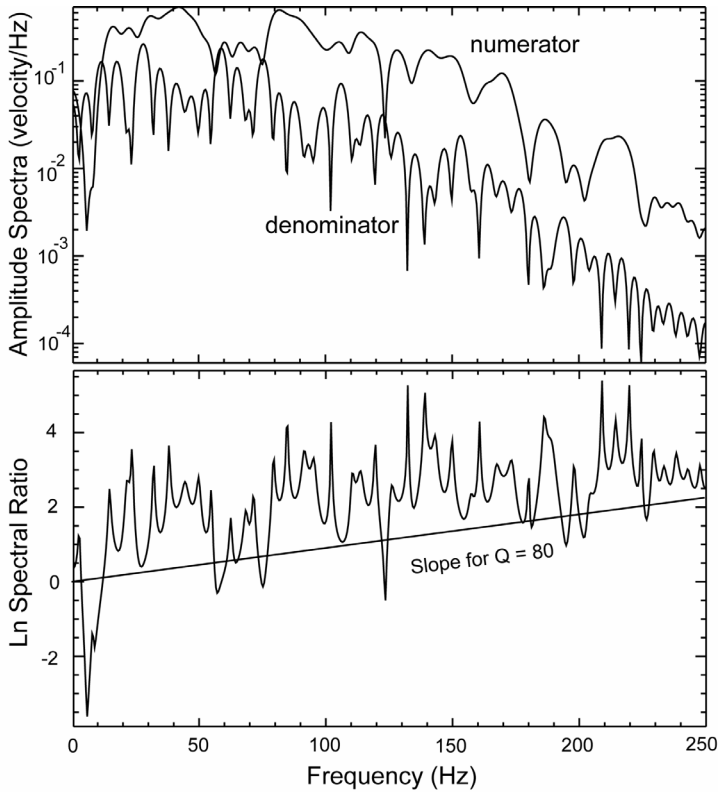

Figure 1.5 Top: Fourier amplitude spectra of the two windowed time series shown in Figure 1.4. Bottom: Natural logarithm of the spectral ratio. The slope for Q = 80, as assumed for the example, is indicated by the straight line.

The variance of the estimates of Q for a given time separation (τ_q-τ_p) can be reduced by averaging of the log-spectral ratios from multiple sources and receivers, as shown below with real data. This multi-channel spectral ratio stacking allows us to take advantage of the large amount of data recorded by the seismic survey.

Near-Offset Data

The method described above was applied to data from shotpoints 22 through 29. Figure 1.6 shows a shot-gather from shotpoint 22. The sections of time series from the various receivers that are potentially useful for analysis are shown as shaded regions in Figure 1.6. The range in offset is from 200 to 2000 meters. For a given value of τ_q-τ_p, the minimum useful offset is determined by the arrival of surface waves. The maximum useful offset for a given τ_q-τ_p is limited by the time between the first arrival of energy and the basement reflection, which decreases with offset. Our estimates of Q from the near-offset data are based on reflections within the sedimentary section using τ_q-τ_p = 0.3 seconds. This value of lapse time was arrived at by extensive testing, and is a compromise between the number of traces available (which increases with smaller values of τ_q-τ_p) and resolution of the slope of the log-spectral ratio versus frequency function (which increases with larger τ_q-τ_p). The optimum value of 0.3 seconds provides 50

spectral ratios for the estimation of Q under the imposed restriction of raypath location outside of the inner crater rim of the impact structure. The mean amplitudes of the time segments were subtracted and the results tapered using a Hanning window to reduce truncation effects and spectral sidelobes. Three other window functions (Bartlett, Hamming, Blackman) were tested. The spectral ratios are not sensitive to the choice of window type.

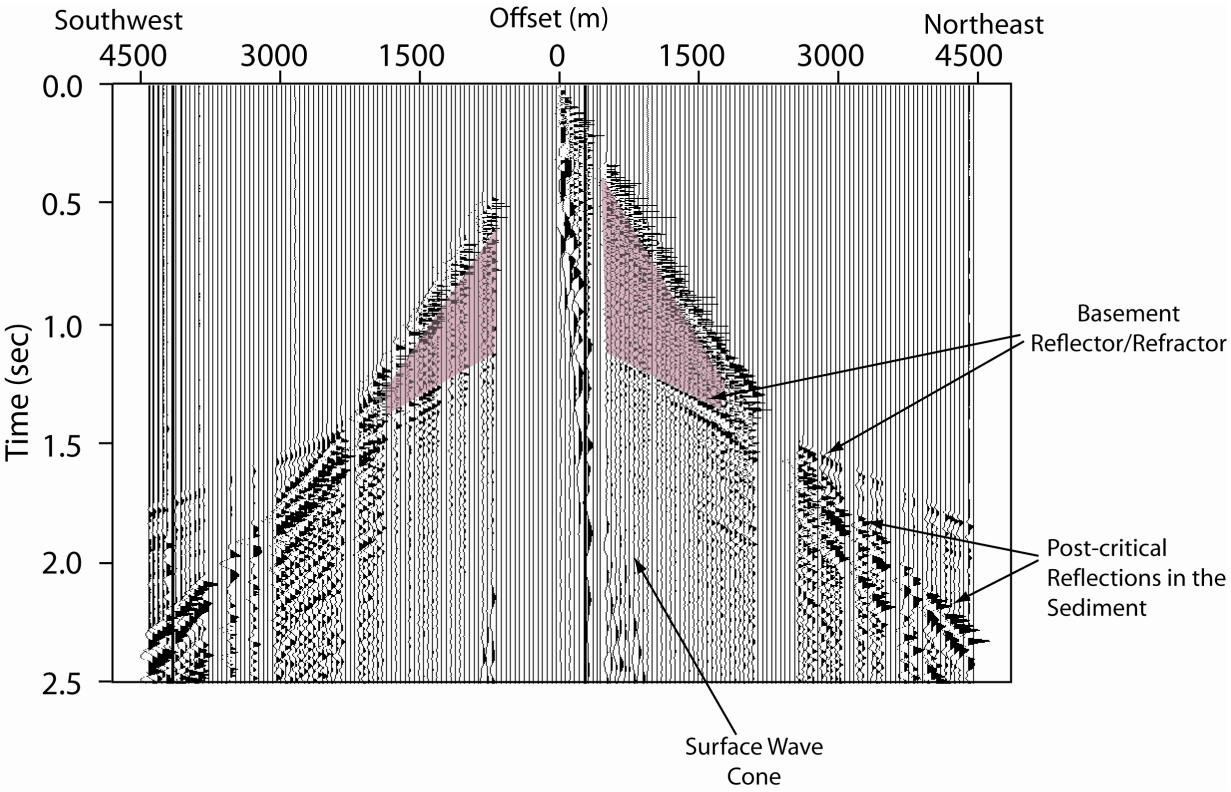

Figure 1.6 Shot-gather from shotpoint 22, to 4500 m source-receiver offset. The shaded area indicates sections of traces processed to estimate Q at near offsets (less than 2000 m). Traces at far offset (greater than 2160 m) feature strong post-critical reflections from the top of basement and from velocity contrasts within the sediment section. Wide-angle, post-critical reflection data at large offsets to the northeast of shotpoints 22-25 were also used to estimate Q from spectral ratios.

Figure 1.7 shows an example seismogram, from shotpoint 24 at a distance of 450 meters, with times τ_p and τ_q indicated. Also shown in Figure 1.7 are the numerator and denominator amplitude spectra and the pre-signal noise amplitude spectrum. The signal-to-noise ratios of the near-offset data are very large, and the usable bandwidth is limited only by the Nyquist frequency (250 Hz). The excellent signal/noise is a result of the quite recording environment, the large charge sizes, and the fact that the charges were completely contained below the shallow water table.

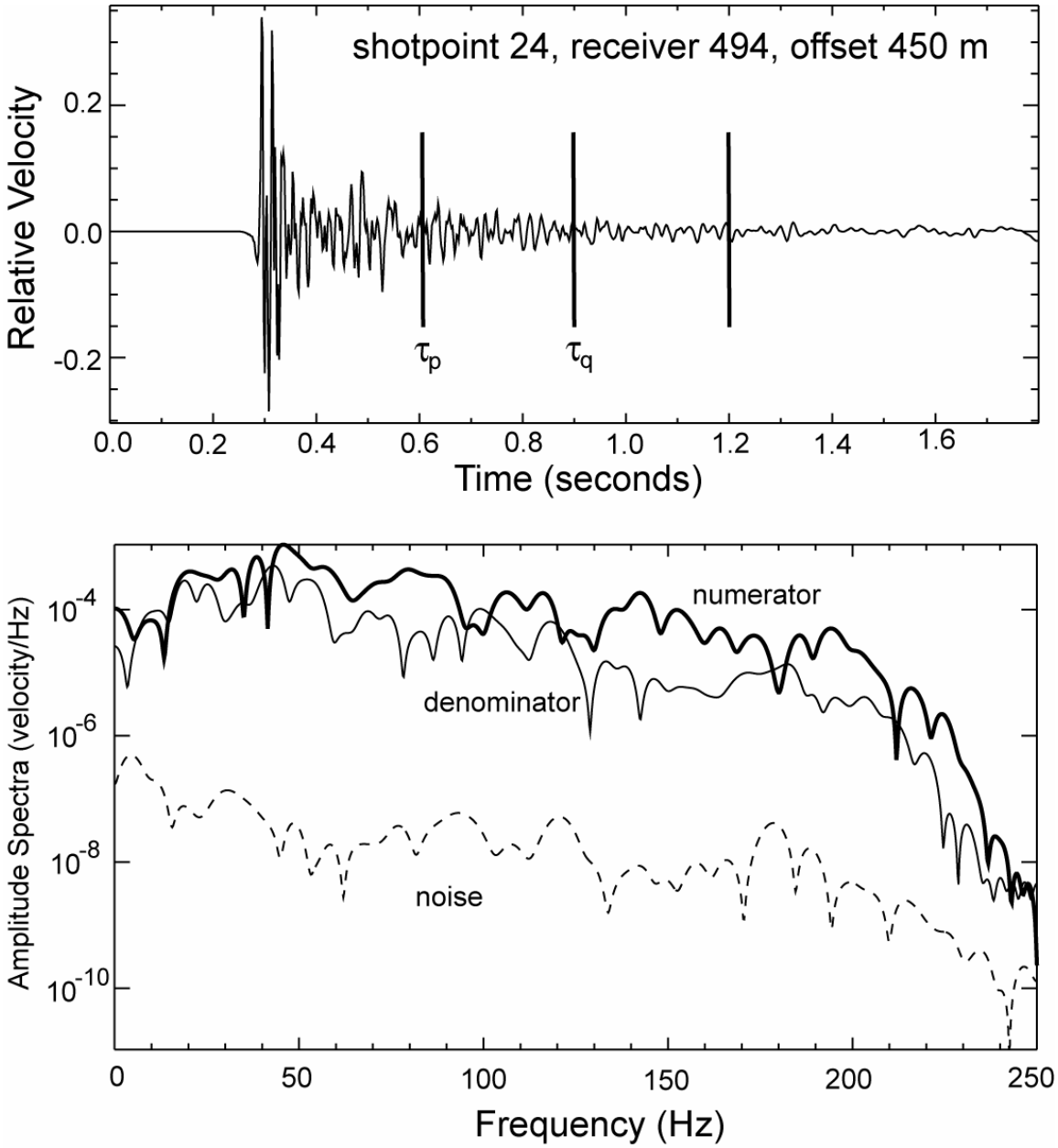

Figure 1.7 Top: recorded data at receiver location 494, from shotpoint 24, at 450 meter offset. Start times for the 0.3 second numerator and denominator windows (τ_p, τ_q) are indicated. The reflection from the top of basement is at 1.2 seconds. Bottom: Fourier amplitude spectra of the numerator and denominator time series, and pre-signal noise (0.3 second time segment).

Figure 1.8 shows the spectral ratio derived at 450 m from shotpoint 24, compared with the result obtained by the multi-channel averaging of the log-spectral ratios from all 50 available recordings at distances less than 2000 m. Figure 1.9 shows the linear regression fit to the average log-spectral ratio versus frequency function. The resulting estimate of Q is 78, based on a regression in the 10 to 150 Hz range. The R^2 value of the regression is 0.89, and a 95% confidence interval for the value of Q is 75 to 80.

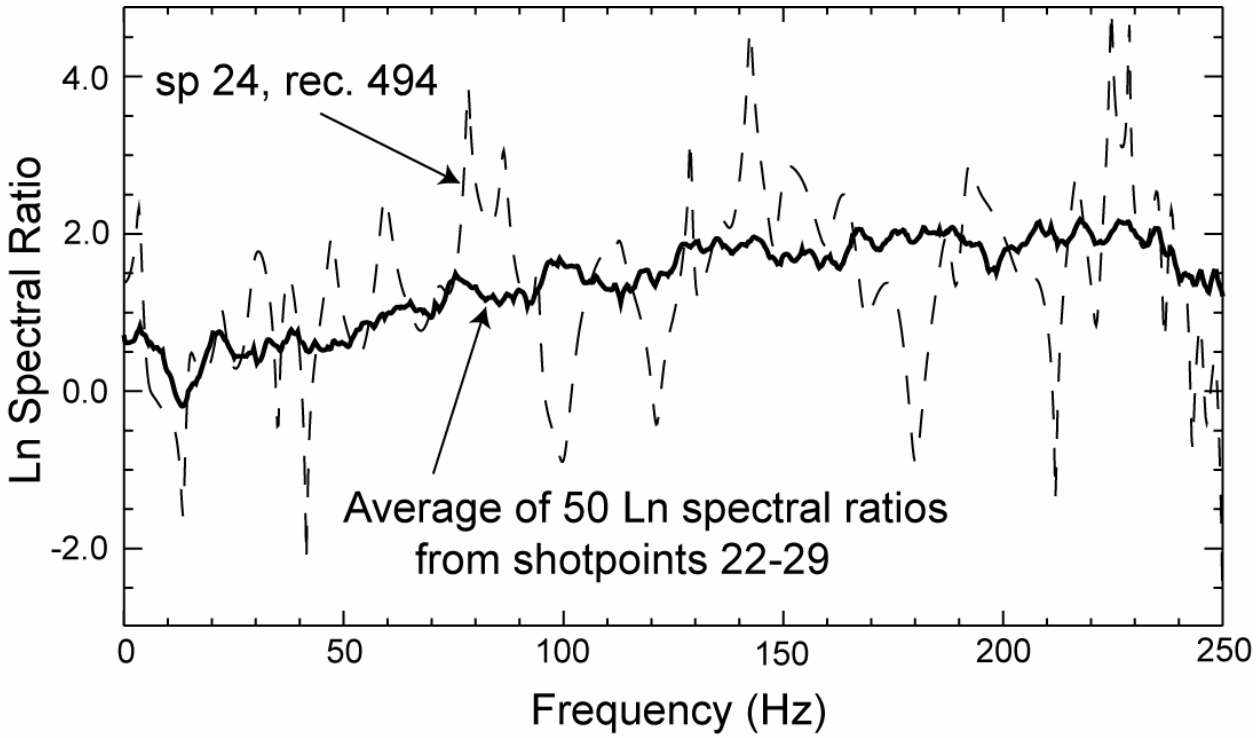

Figure 1.8. The dashed line shows the natural logarithm of the spectral ratio derived from the single trace recorded at receiver 494, from shotpoint 24. The thick solid line shows the result of averaging the full suite of near-offset log-spectral ratios, comprised of 50 values with $\tau_q - \tau_p$ equal to 0.3 seconds. Note that the averaging greatly reduces the variance of the spectral ratio estimate derived from a single trace.

A histogram of the 50 estimates of Q derived from regressions of the individual spectral ratios is shown for comparison in Figure 1.9. The values range from a minimum of 30 to a maximum of 185. The median value of 78 agrees with the preferred result derived from the slope of the average log-spectral ratio versus frequency function. Note that the distribution of individual estimates of Q exhibits four outliers with values in the range 150 to 200. As a result, the mean of the individual estimates, 99, is larger than the median and the standard deviation of the individual measurements is large: 70. The 95% confidence interval for Q (i.e., 95% confidence interval for the mean of the individual measurements) is 79 to 118. If we delete the outlier values (those greater than 150 shown in Figure 1.9), the mean of the individual estimates of Q is 78, the standard deviation of the measurements is 25 and the 95% confidence interval for the mean is 70 to 85, in much better agreement with the results derived from the regression of the multi-channel average.

The agreement of the results derived from the regression of the average of 50 log-spectral ratios with the central tendency of the distribution of the individual estimates is interpreted to indicate that the estimate of Q based on the average of spectral ratios is robust, unbiased, and therefore is to be preferred over the results based on the individual regressions of the log-spectral ratios, because of the smaller variance in the estimate of Q.

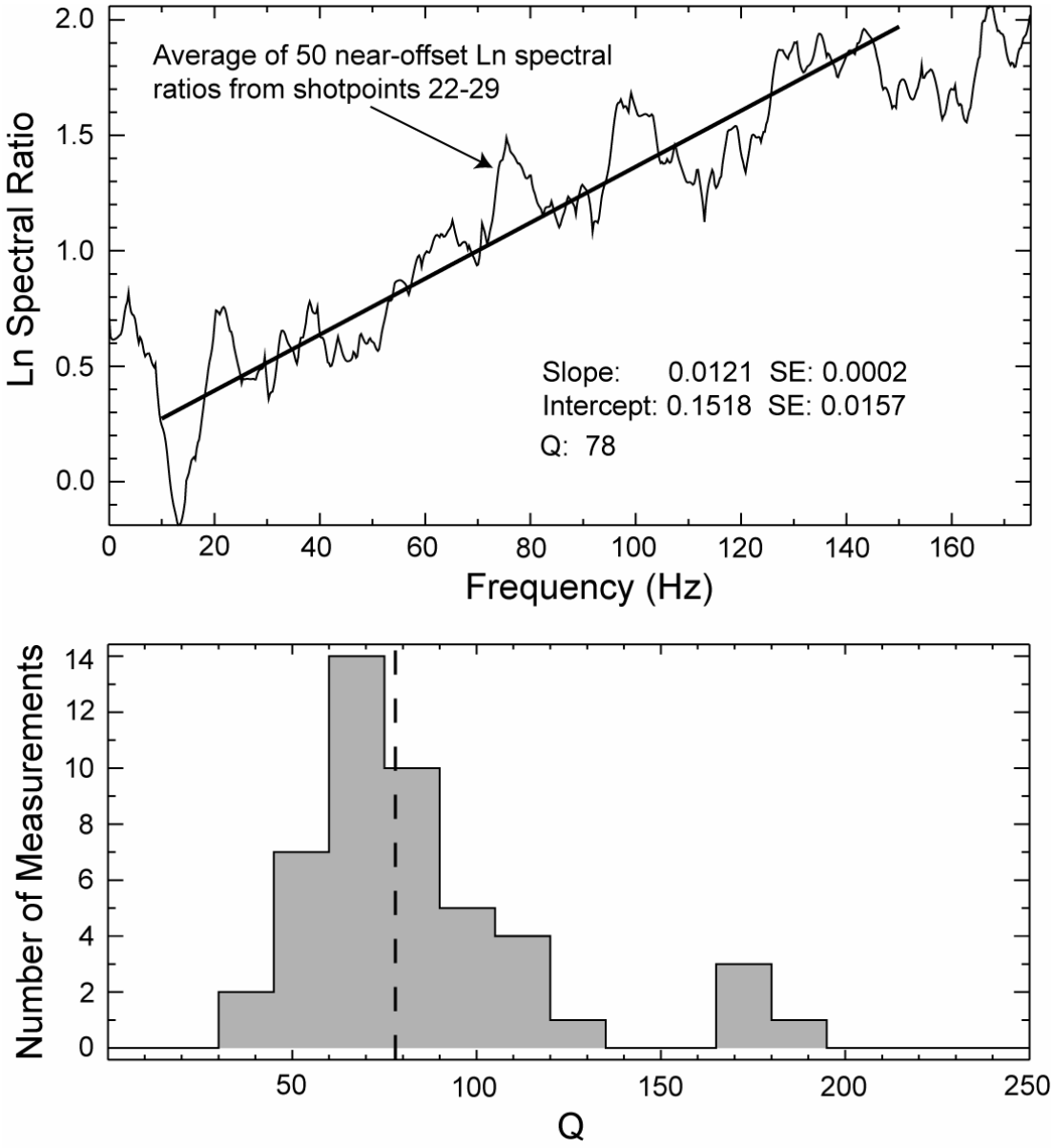

Figure 1.9 Top: Linear regression fit to the average log-spectral ratio derived from 50 near-offset traces with $\tau_q - \tau_p$ equal to 0.3 seconds. The fit is performed between 10 and 150 Hz. The slope indicates a value for Q of 78. SE is standard error of estimate. Bottom: histogram of Q estimates derived from linear regression fits to each of 50 individual log-spectral ratios at near offsets. The dashed line shows the median value: 78, in agreement with that derived from the average spectral ratio.

The time intervals used for this analysis begin after the arrival of the strong reflection from the top of the Exmore beds, (top of the syn-impact units) and end with the arrival of the basement reflection. Thus the estimates of Q are representative of the attenuation in the syn-impact deposits.

The slope of the average log-spectral ratio shown in figures 1.8 and 1.9 changes in the vicinity of 150 Hz, and becomes essentially flat between 175 and 225 Hz. This does not

appear to be an effect of recording system dynamic range, or signal-to-noise ratio, based on attempts to simulate the observation numerically. We interpret this to indicate that apparent attenuation decreases markedly at frequencies above 150 Hz, for the lapse time examined here, and that Q becomes an increasing function of frequency at the highest frequencies. This has implications for the physical mechanism of attenuation that are beyond the scope of the present study. We speculate that the data suggest a change from single-scattering for frequencies less than approximately 150 Hz to multiple scattering at higher frequency. The motivation of the study is to estimate Q in the frequency range of primary engineering concern (e.g., frequencies in the range 1 to 30 Hz). Our data cannot resolve Q at frequencies less than approximately 10 Hz because of the short (0.3 sec) lapse times, but the linear trend of the log-spectral ratio at frequencies between 10 and 150 Hz gives us some confidence that our assumption of frequency independent Q holds for the frequency range of engineering concern.

Far-Offset Data

Prominent secondary arrivals at distances exceeding approximately 2000 m are apparent in Figure 1.6. These arrivals are wide-angle reflections from the basement, and from within the sedimentary section. At large offsets, multiple reflections create a horizontally guided wave group traveling within the sediments with a velocity of approximately 2.0 km/s. The amplitude decay of these waves can be used to estimate Q within the sedimentary section (Langston et al., 2005).

We use these sediment-guided P-waves generated at shotpoint 22 in the offset range 2.6 to 6.5 km to get another estimate of Q. The approach is again based on the spectral ratio of two windowed time segments. In this case, the numerator spectrum Y_p and denominator spectrum Y_q in Equation 2 must be taken from different receivers. In doing this, we lose one of the main advantages of the analysis approach described above for treatment of the near-offset reflection data. In forming the spectral ratio using data from two different stations at large offset, any frequency-dependent instrument response differences or receiver effects due to near-surface velocity differences at the two receiver sites will not cancel in the spectral ratio. Instrument response variability is not likely to be significant because identical geophones were used for the seismic survey. However, as noted by Langston (2003a, 2003b), near-surface effects can introduce an error in the estimate of Q. Even if the estimates are not systematically biased by near-surface variability, we expect an increase in the scatter of a group of measurements due to that effect.

Figure 1.10 shows examples of the far-offset seismograms, at offsets of 2.6 and 6.5 km. Also shown in Figure 1.10 are synthetic seismograms computed using the frequency-wavenumber integration method. The synthetics were generated using the velocity model shown in Figure 1.3, with Q_p and $Q_s = 80$. We consider them to be in good agreement with the real data, in terms of frequency content, amplitude and general appearance of the body waves. For example, the arrival-time and duration of the P-wave group guided within the sedimentary sequence increases with offset, an observation modeled accurately in the synthetics. The duration of the time segments used to form the numerator and denominator spectra must vary with offset. The time separation τ_q-τ_p needed to estimate Q from the slope of the log-spectral ratio is reckoned between the centers of the time segments that include the sediment-guided P-wave arrivals.

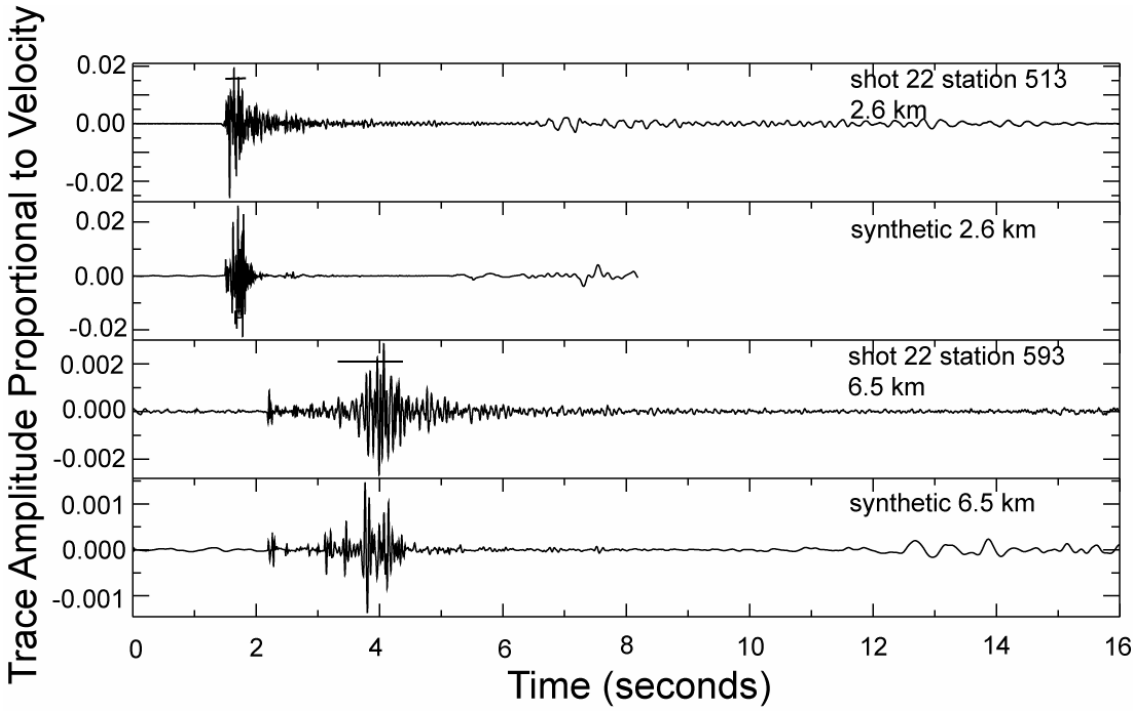

Figure 1.10 Example of data used to estimate Q from wide-angle reflections at far offset, showing recorded data and full-wavefield synthetics for offsets of 2.6 and 6.5 km, respectively. Horizontal lines indicate time windows used to form spectral ratios.

Figure 1.11 shows the Fourier amplitude spectra of the wide-angle reflections and pre-signal noise calculated from the seismograms shown in Figure 1.10. The corresponding log-spectral ratios are shown in Figure 1.12. Similar calculations were performed for 136 receiver pairs in the offset range 2.6 to 6.5 km. The high-frequency limit of the linear regression analysis used to estimate Q from the slope of the log-spectral ratio is determined by the signal-to-noise ratio of the data at the larger offsets, and was decided on a case-by-case basis. For example, the data shown in Figure 1.11 are bandlimited by noise to frequencies less than 80 Hz at the far offset of 6.5 km, and the regression in that case was performed over the frequency range 10 to 80 Hz.

The difference in lapse times among the individual spectral ratios derived from the far-offset data does not permit the averaging of multiple spectral ratios. A histogram of the estimates of Q derived from linear regression of all the individual spectral ratios developed from the far-offset data is shown in Figure 1.13. The mean and median estimates are 92 and 93, respectively, and the standard deviation is 35. The 95% confidence interval for the mean is 86 to 98. Thus, the far-offset data imply a somewhat larger Q for energy propagating as wide-angle reflections, compared to the estimate of Q (75-80, at 95% confidence) based on the multi-channel stacking of the near-offset data.

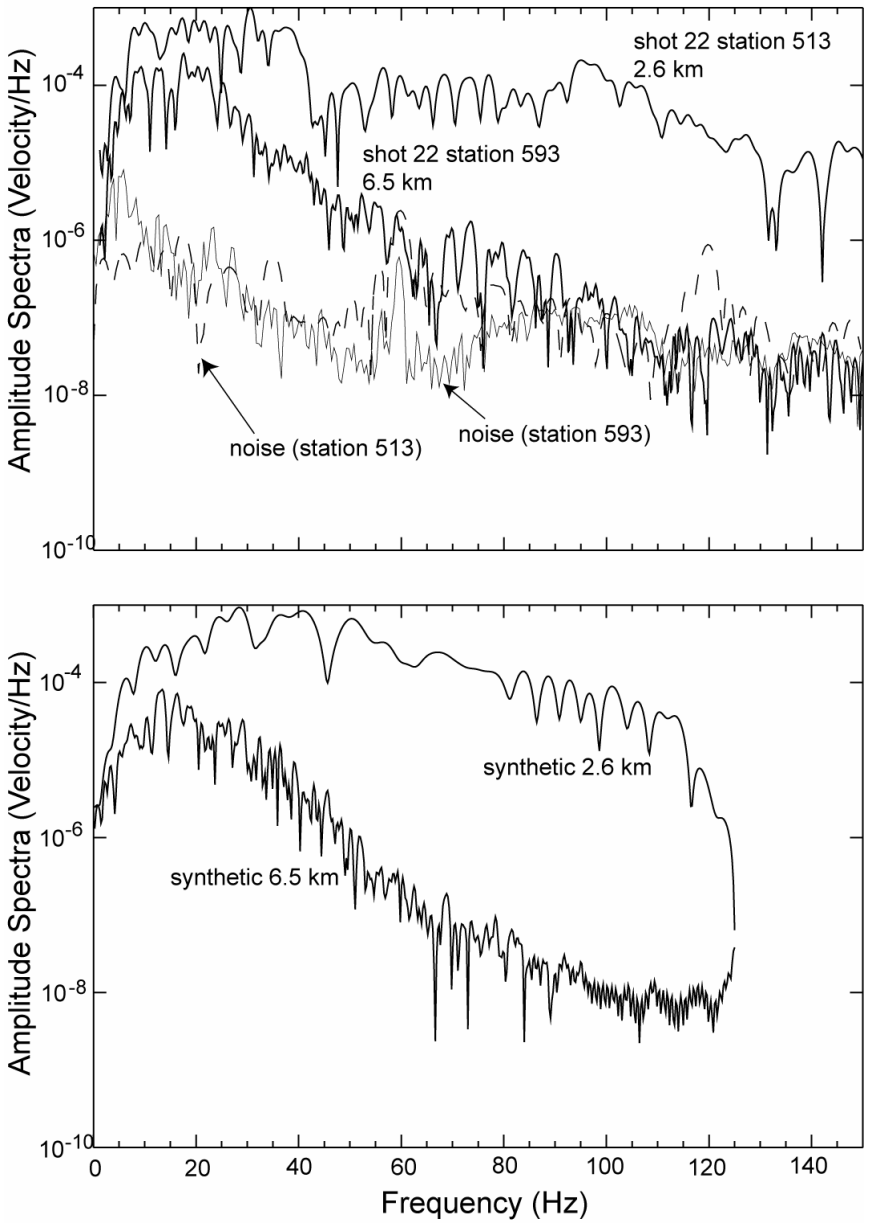

Figure 1.11 Top: Amplitude spectra of post-critical reflections at offsets of 2.6 km and 6.5 km, from shotpoint 22, with pre-signal noise spectra. Bottom: Amplitude spectra derived from synthetic seismograms.

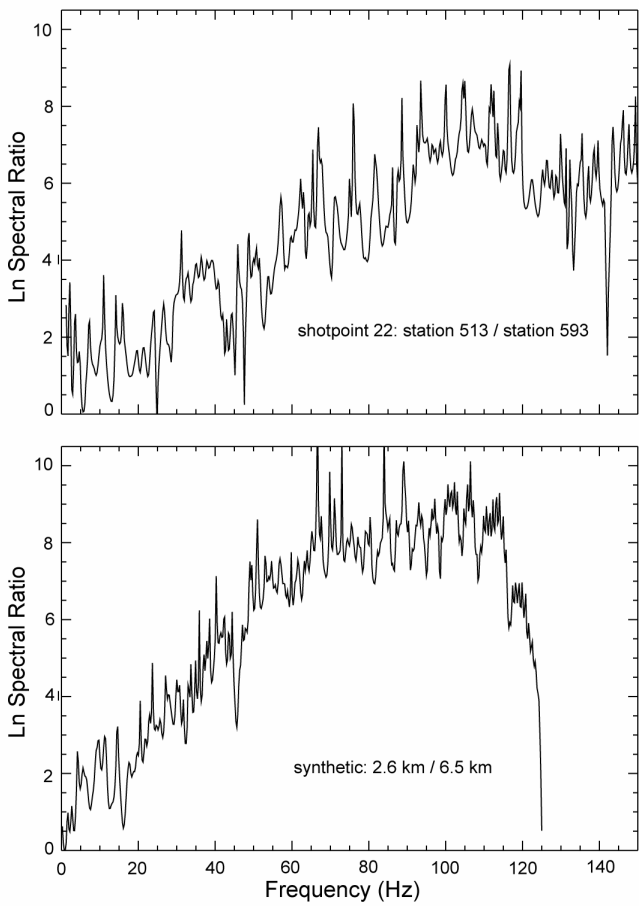

Figure 1.12 Top: Log-spectral ratio from post-critical reflections recorded at stations 513 and 593 at offsets of 2.6 and 6.5 km, respectively. Bottom: Log-spectral ratio derived from synthetic seismograms.

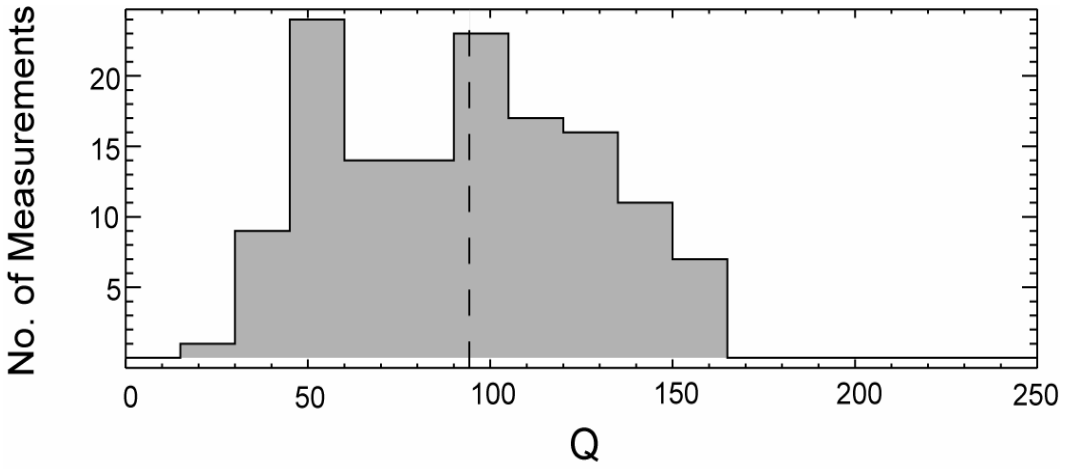

Figure 1.13 Histogram of 136 individual estimates of Q using post-critical reflections from receivers at offsets in the range 2.6 to 6.5 km. The dashed line shows the median estimate: 93. The mean estimate is 92, and standard deviation is 35.

Conclusions

The estimates of Q for P-waves in the Atlantic Coastal Plain sediments derived by this study are in the range 75 to 100. We consider a value of 80 based on log-spectral ratio averaging of reflection data at near-source offsets as a representative best estimate, free from bias due to source and receiver effects, as well as any assumption and/or corrections concerning geometrical spreading. The value is approximately twice that previously reported by Chapman et al. (2003) for the Coastal Plain near Charleston, South Carolina, and also exceeds values reported by many other investigators in similar sedimentary environments. The value is a representative measurement for the section of deeper sediments (e.g., below 300 meters) for frequencies in the range 10 to 150 Hz. There appears to be no significant frequency dependence of Q within that frequency range, but the data suggest that Q increases markedly at higher frequencies. Our data are not capable of resolving Q at frequencies less than 10 Hz.

The estimate of Q found here is a little less than one-half that reported by Langston et al. (2005) for P-waves in the Mississippi Embayment. This study differs from that of Langston et al. (2005) in many ways, including analytical approach, frequency range of the data and type of wave studied. In particular, this study does not examine surface wave propagation at long range. Experimental differences aside, the study areas are different despite gross geologic similarities. On the one hand, the velocities of the sedimentary deposits in both areas at similar depths are similar, and the Lower Tertiary and Cretaceous sediments comprising the bulk of the deposits in both areas were originally nearly the same in terms of geological provenance. Post-Eocene deposits in both areas are geologically similar as well. However, the Eastern Shore of Virginia was disturbed in the Late Eocene by a major asteroid or comet impact. The possibility that this could substantially increase the intrinsic attenuation of the deeper, Lower Tertiary and Cretaceous sediments without significantly affecting the velocity would seem unlikely, but perhaps this contributes to the difference in estimates of Q found by the two studies.

Acknowledgments

This study would not have been possible without the generous assistance of Rufus Catchings and Mark Goldman of the U.S. Geological Survey, Menlo Park, California.

.

References
Part 1

Abercrombie, R.A. (1997). Near surface attenuation and site effects from comparison of surface and deep borehole recordings, Bull. Seism. Soc. Am., 87, 731-744.

Boore, D. M., J.F. Gibbs, W.B. Joyner, J.C. Tinsley and D.J. Ponti (2003). Estimated ground motion from the 1994 Northridge, California, earthquake at the site of the Interstate 10 and La Cienega Boulevard Bridge collapse, West Los Angeles, California, Bull. Seism. Soc. Am, 93, 2737-2751.

Catchings, R.D., D.S. Powars, G.S. Gohn, and M.R. Goldman (2005).High-Resolution Seismic-Reflection Image of the Chesapeake Bay Impact Structure, NASA Langley Research Center, Hampton, Virginia, chap. I of Horton, J.W., Powars, D.S. and Gohn, G.S., eds., Studies of the Chesapeake Bay impact structure -The USGS-NASA Langley corehole, Hampton, Virginia, and related coreholes and geophysical surveys: U.S. Geological Survey Professional Paper 1688, p. I1-I21.

Chapman, M.C., P. Talwani, and R.C. Cannon (2003). Ground-motion attenuation in the Atlantic Coastal Plain near Charleston, South Carolina, Bull. Seism. Soc. Am., 93, 998-1011.

Gohn, G.S., D.S. Powars, T.S. Bruce and J.M. Self-Trail (2005). Physical Geology of the Impact-Modified and Impact-Generated Sediments in the USGS-NASA Langley Core, Hampton, Virginia, chap. C of Horton, J.W., Powars, D.S. and Gohn, G.S., eds., Studies of the Chesapeake Bay impact structure -The USGS-NASA Langley corehole, Hampton, Virginia, and related coreholes and geophysical surveys: U.S. Geological Survey Professional Paper 1688, p. C1-C38.

Herrmann, R.B. (2002). Computer Programs in Seismology: An Overview of Synthetic Seismogram Computation. Department of Earth and Atmospheric Sciences, St. Louis University, St. Louis Missouri, 183 p. Version 3.30 software and documentation available at URL *http://www.eas.slu.edu/People/RBHerrmann/ComputerPrograms.html.*

Horton, J.W., D.S. Powars, and G.S. Gohn (2005). Studies of the Chesapeake Bay impact structure - Introduction and Discussion, chap. A of Horton, J.W., Powars, D.S. and Gohn, G.S., eds., Studies of the Chesapeake Bay impact structure -The USGS-NASA Langley corehole, Hampton, Virginia, and related coreholes and geophysical surveys: U.S. Geological Survey Professional Paper 1688, p. A1-A23.

Langston, C.A., P. Bodin, C. Powell, M. Withers, S. Horton and W. Mooney (2005). Bulk sediment Q_p and Q_s in the Mississippi Embayment, Central United States, Bull. Seism. Soc. Am. 95, 2162-2179.

Langston, C.A. (2003a). Local earthquake wave propagation through Mississippi Embayment sediments, Part I: Body-wave phases and local site response, Bull Seism. Soc. Am., 93, 2664-2684.

Langston, C.A. (2003b). Local earthquake wave propagation through Mississippi Embayment sediments, Part II: Influence of local site velocity structure on Qp-Qs determinations, Bull Seism. Soc. Am., 93, 2685-2702

Liu, Z., M.E. Wuenscher and R.B. Herrmann (1994). Attenuation of body waves in the central New Madrid Seismic Zone, Bull. Seism. Soc. Am., 84, 1112-1122.

Powars, D.S., T.S. Bruce, L.E. Edwards, G.S. Gohn, J.M. Self-Trail, R.E. Weems, G.H. Johnson, M.J. Smith and C.T. McCartan (2005). Physical Stratigraphy of the Upper Eocene to Quaternary Postimpact Section in the USGS-NASA Langley Core, Hampton, Virginia, chap. G of Horton, J.W., Powars, D.S. and Gohn, G.S., eds., Studies of the Chesapeake Bay impact structure -The USGS-NASA Langley corehole, Hampton, Virginia, and related coreholes and geophysical surveys: U.S. Geological Survey Professional Paper 1688, p. G1-G44.

Wessel, P., and W.H.F. Smith (1998). New improved version of Generic Mapping Tools released, Eos, Transactions of the American Geophysical Union, 79, 579.

Part 2

Cenozoic Faulting Imaged in the Epicentral Area of the 1886 Charleston, South Carolina Earthquake: Results of Reprocessing Seismic Reflection Line VT-3b

Grant Awards 06HQGR0109 & 07HQGR0042

Introduction

Data from seismic reflection profiles acquired by the Virginia Tech Regional Geophysics Laboratory, in a collaborative study with the U.S. Geological Survey, were initially to form the basis for the estimation of Q described above in Part 1 of this report. These data were collected in 1980-1981 near Summerville, South Carolina and consist of 5 profiles, ranging in length from approximately 5 to 15 km. The seismic source was a Failing Y1100 truck-mounted vibrator (125-kN peak force). The 48-channel vertical component data were collected with typical receiver spacing of 35 meters at 500 Hz sample rate. The recorded vibrator frequency sweep was from 10 to 80 Hz.

Work completed under grant number 06HQGR0109 involved data retrieval from original tapes and the assembly of the data set in formats suitable for analysis on modern platforms and software. Data from lines VT-1 through VT-4 were transferred from original magnetic tapes in DISCO proprietary format to SEGY format on hard disk and DVD. Shot-receiver geometry was assembled from field notes and archives, and embedded into the SEGY files. The data were cross-correlated with the vibrator sweeps and the results were archived in SEGY format. Shot gathers from lines VT-1, VT-2, VT-3b and VT-4 were examined using the ProMAX seismic processing package (a product of Landmark, Inc.) and the highest quality data set extracted for Q analysis following the approach described above in Part 1 of this report. As the work progressed, it became apparent that the decrease in data variance expected by the stacking of multi-channel log-spectral ratio versus frequency functions was not occurring, due to complex modulation of the recorded amplitude spectra. We determined that the source of the modulation was the recording geometry, which employed large-spacing receiver arrays.

The receiver arrays were designed to improve the subsurface image by allowing the incorporation of near-offset data in the common-mid-point (CMP) stacking. As will be demonstrated below, this element of the survey design was very successful. The result is a clear image of significant faulting involving the Mesozoic and Cenozoic section to within 100 meters of the surface, along the north side of the Ashley River, opposite the place known as Gregg's Landing, in the epicentral tract of the 1886, Charleston, South Carolina earthquake.

Anomalous Events on Line VT-3b

Strong events exhibiting reverse moveout were discovered during the course of examining individual shot-gathers on line VT-3b. Figure 2.1 shows an example of one of the features.

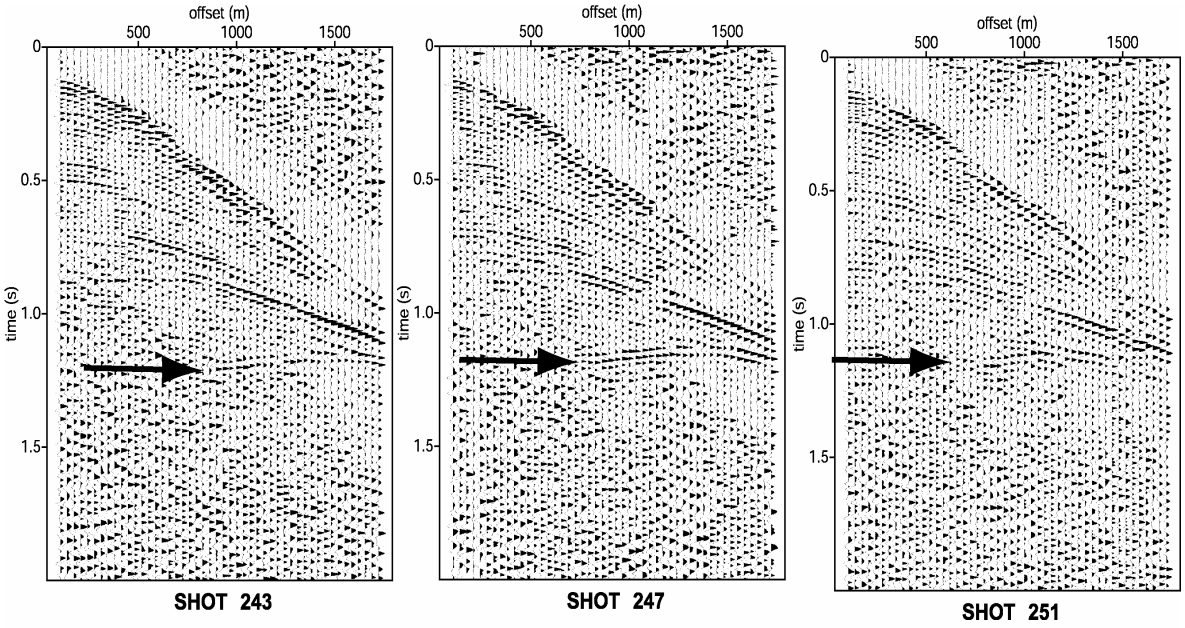

Figure 2.1 Shot gathers on line VT3b from shotpoints 243, 247 and 251, showing strong-amplitude events with reverse moveout, indicated by arrows.

The event shown in Figure 2.1 was initially interpreted as either a diffraction from a point, or possibly due to a reflection and subsequent refraction of energy from a steeply dipping reflector. As indicated in Figure 2.1, the event is observed on many shots at a fixed receiver ground position, indicating the approximate subsurface position of the point of diffraction or reflector. The location is in coincidence with modern earthquake activity, historical accounts of maximum intensity effects and locations of ground disruption noted in 1886. This motivated us to carefully study these events and completely reprocess line VT-3b in an effort to identify the nature of the events and better resolve the image of sub-surface structure along that profile.

Study Area

Figure 2.2 is a map of the study area, showing instrumentally located earthquake epicenters derived by the University of South Carolina Seismic Network and reported in the Southeastern United States Seismic Network Bulletins and catalog, compiled and maintained by Virginia Tech (URL ***http://www.geol.vt.edu/outreach/vtso/***). The map also shows the locations of the 1981 Virginia Tech seismic profiles (VT-1 through VT-5), and profiles acquired in 1979 by the U.S. Geological Survey (SC lines), along with the mapped locations of liquefaction, ground disruption and displacement of railroad track caused by the 1886 earthquake, reported by Dutton (1889). Dutton's dual epicenters are also indicated in Figure 2.2.

Figure 2.2 shows that most of the reflection data were collected along roads to the west and north of the 1886 ground disruption features and areas of the most significant

modern seismicity. Fortunately, seismic lines SC-6, VT-5, VT-3b, VT-1, SC-10 and SC-4 imaged the subsurface in the vicinity of the mapped ground disruptions and earthquake activity, but with variable resolution. Lines VT-3b, VT-1 and SC-10 are particularly interesting, because they run approximately parallel to one another on either side of the Ashley River, and sample the zone of most significant recent seismicity.

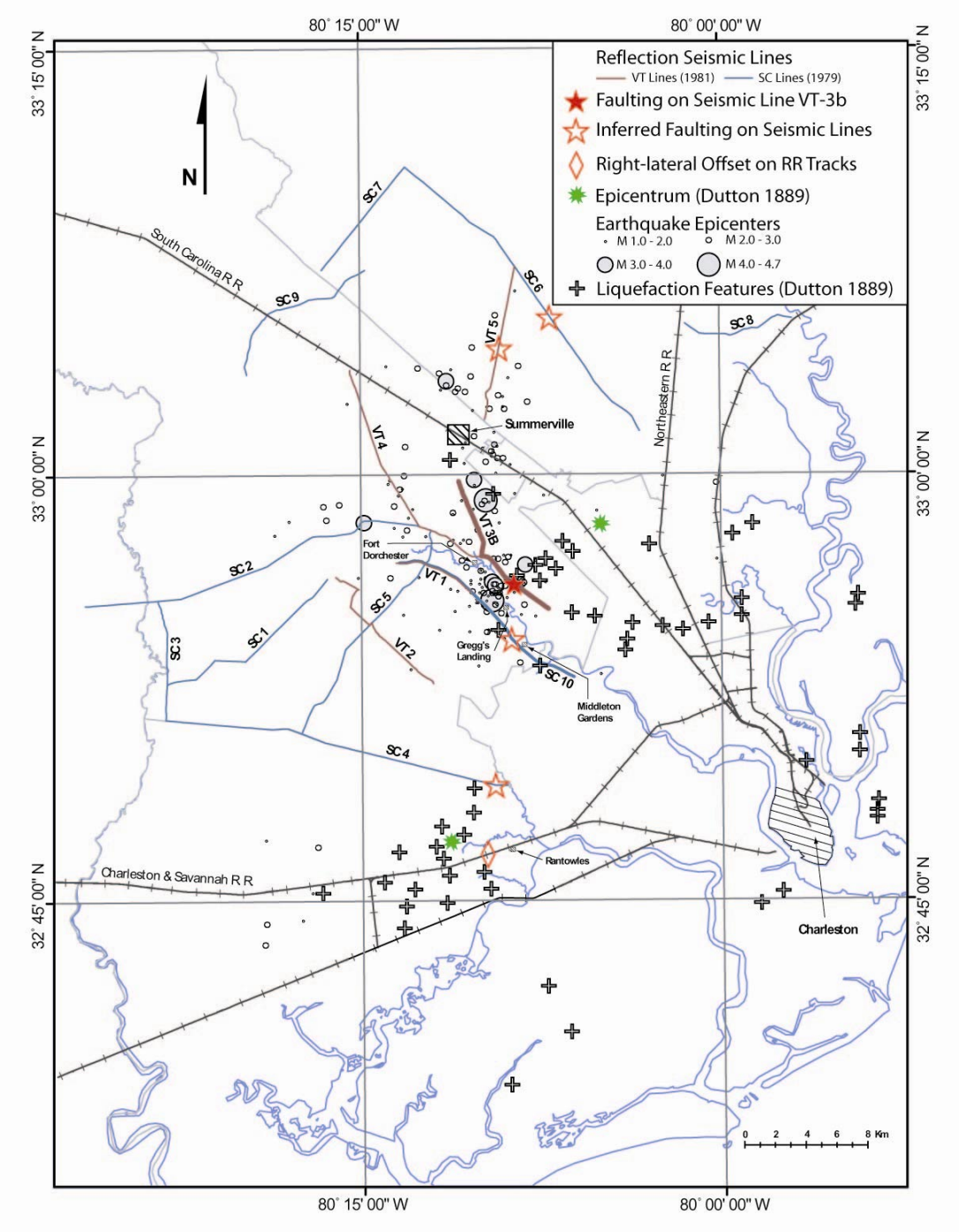

Figure 2.2 Map of the study area.

The Data

The following description of the acquisition parameters is specific to line VT-3b and is summarized in Table 1. The line location is shown in Figure 2.2.

	VT3b
Record Time (sec)	21
Sample Rate (ms)	2
Spread Geometry	Off-end
Fold	24
Receiver Group Interval (m)	35
Near Source Offset (m)	70
Number of Vibrators	1
Number of Sweeps per Vibrator Point	16
Sweep Length (sec)	19
Sweep Frequency Band (Hz)	80-10

Table 2.1 Acquisition parameters for reflection-seismic data from line VT3b.

Reprocessing

Line VT-3b was originally processed in 1981 using then-standard reflection processing techniques with only minor variations (Çoruh et al., 1981). The reprocessing of line VT-3b undertaken in this study consisted of the following steps:

1) Crooked line geometry assignment,

2) Standard VIBROSEIS cross-correlation with the pilot sweep,

3) Trace edit and mute of non-reflection energy,

4) Geometric spreading and attenuation correction,

5) Inverse filter to convert the zero-phase Klauder wavelet to minimum-phase,

6) Bandpass filter 16-24-58-80 Hz,

7) Minimum-phase, spiking deconvolution followed by trace balance and final noise mute,

8) Bandpass filter 16-24-58-80 Hz,

9) Elevation static correction and common mid-point (CMP) sort,

10) Velocity analysis (10 CMP interval) - two iterations of velocity picks and residual static correction,

11) NMO correction and stretch mute followed by CMP stack with smoothed velocity model.

Figure 2.3 compares the original, unmigrated CMP stacked section of line VT-3b with the reprocessed, unmigrated CMP stack. After each of the steps listed above, the results were examined in the time and/or frequency domain to assess improvement. Stacks were produced with and without application of pre-stack, predictive deconvolution. The pre-stack decovolution did not effectively suppress multiple reflections, and therefore was not included in the final processing sequence. Post-stack migration (in both time and depth) was performed. The common migration algorithms were tested with only minor differences in results. Migration resulted in little change to the image of the sub-surface, compared to that resolved in the CMP stack. Varying the percentage of normal move-out (NMO) stretch mute was tested, and this strongly affected the amplitude of the strong reflection around 0.7 second two-way time on the southeastern half of the profile. This is due to the predominance of far-offset energy for this reflection along that part of the profile compared to the northwestern segment in which near-offset energy is stronger. To compensate, the stretch mute allowance was increased, which slightly degraded the remaining portions of the stack, especially the shallow section. The processing steps which yielded the most improvement compared to the original image were the minimum-phase correction and the spiking deconvolution. Those processing techniques significantly increased the resolution of the data by shortening the wavelet and eliminating the ringing appearance of the reflections.

Figure 2.3 demonstrates the improvement of the CMP stack. The resolution of the shallow section (< 0.3 sec) and the sequence of reflections below 0.7 sec was increased. A remarkable improvement in the lateral continuity of the reflecting horizons was achieved.

Geologic Interpretation of the Data

Figure 2.4 is an annotated version of the reprocessed CMP stacked section. The main geologic features are indicated. The reflections labeled K, J and B follow the nomenclature used in several previous publications dealing with the seismic stratigraphy of the study area (Yantis et al. 1983, Schilt et al. 1983, Behrendt et al. 1981, Hamilton et al. 1983).

The shallowest reflections at approximately 0.1 second two-way time represent contrasting units within the Santee limestone of Eocene age. The "K" reflection package is interpreted by Schilt et al. (1983) as lithologic variation within the Upper Cretaceous Black Creek formation. The strongest reflector on the northwestern part of the profile is labeled "J" by Schilt et al. (1983). It correlates with the unconformable contact between Upper Cretaceous sediments and Jurassic basalt (Hamilton et al. 1983). The radiometric age of the basalt obtained by Lanphere (1983) is 184 +/- 3.3 my. RMS velocities above the basalt increase from 1.97 km/sec at a depth 50 m to 2.13 km/sec at the base of the Cretaceous sediments, based on the sonic log obtained in the Clubhouse Crossroads #1 borehole (Yantis et al. 1983). Clubhouse Crossroads holes #1 and #2 both terminated in the basalt. Clubhouse Crossroads #3 passed through 256 m of basalt between 775 and 1,031 meters, below which it penetrated 121 m of sedimentary red-beds to total depth of 1,152 m (Gohn 1983). Clubhouse Crossroads #3 is the only borehole of which we are aware that has completely penetrated the basalt in the study area. The locations of the three Clubhouse Crossroads holes are near the intersection of lines SC-1 and SC-3 in Figure 2.2.

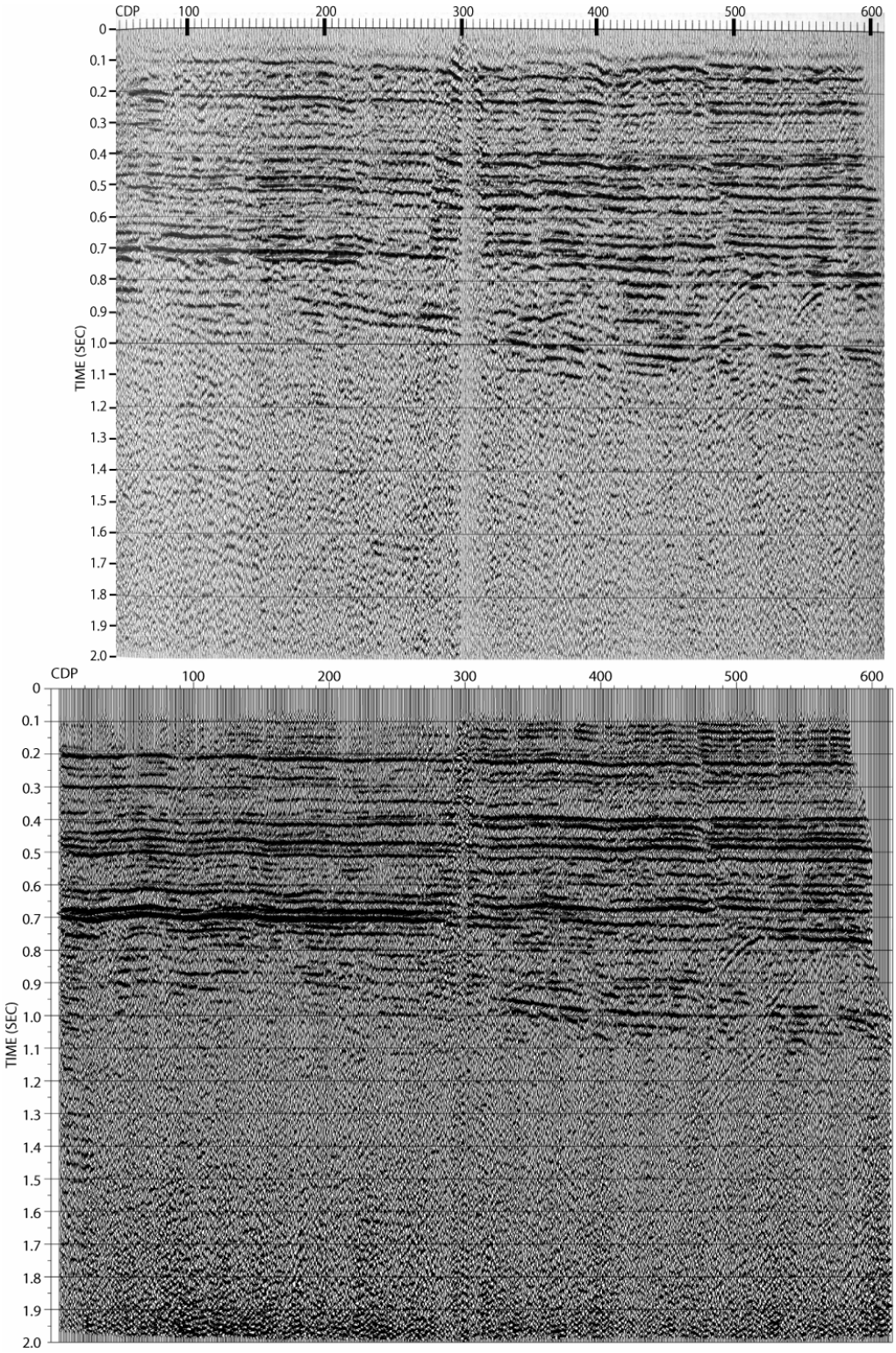

Figure 2.3 Top: original CMP stacked section of line VT-3b. Bottom: Reprocessed VT-3b CMP stacked section.

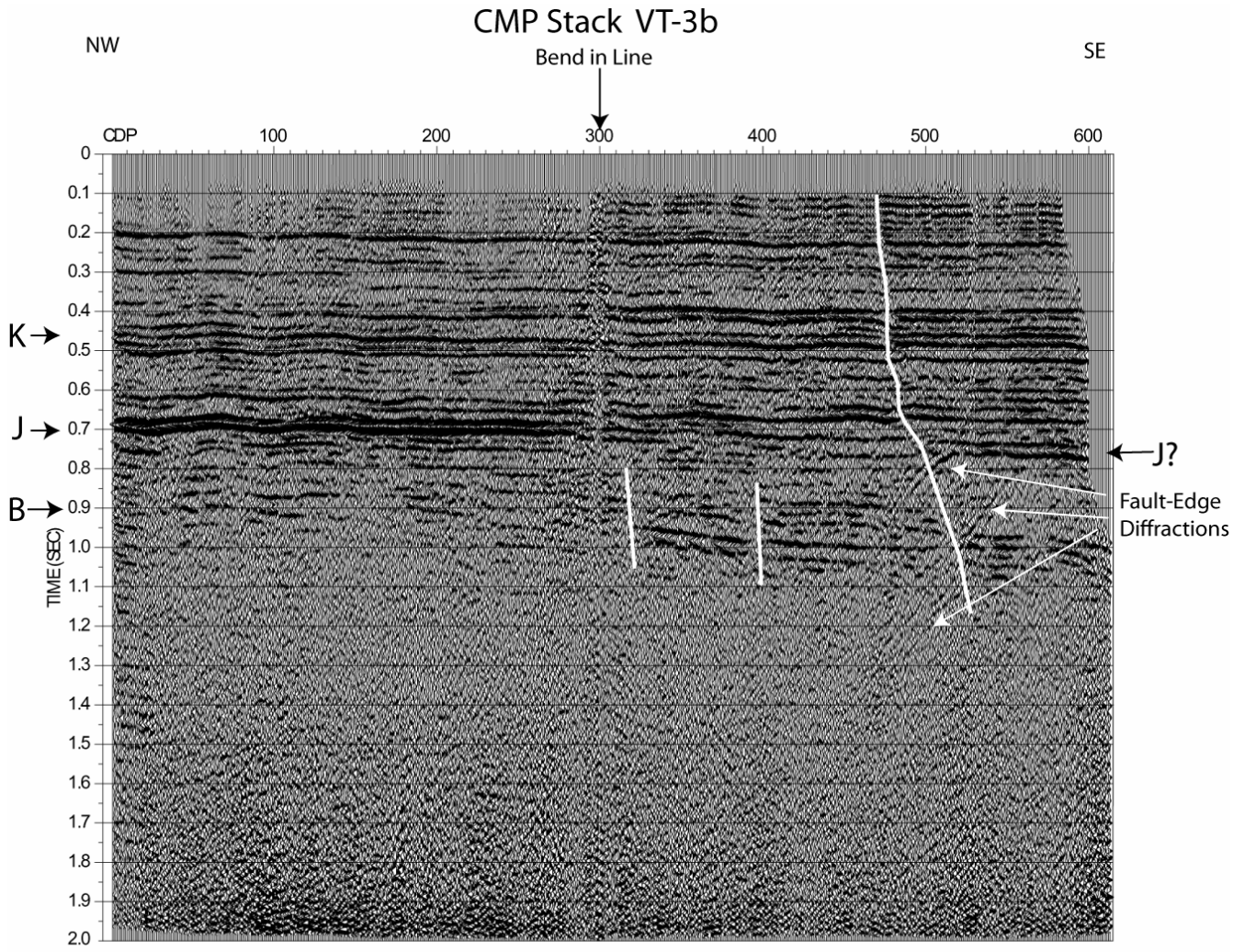

Figure 2.4 Reprocessed CMP stacked section of line VT-3b. Conspicuous reflectors K, J and B are identified using the nomenclature of previous studies. White lines indicate faults. The arrows point to the strongest examples of diffractions from the faulted edges of units with contrasting acoustic impedance.

The "B" label was applied by Schilt et al. (1983) who interpreted a reflection at 0.85 - 0.95 seconds on a COCORP reflection line in the study area as due to the contact between "basement" and Mesozoic sedimentary rock.

The northwestern half of the reprocessed profile shown in Figure 2.4 shows a sequence of horizontal reflections, between 0.7 and approximately 1.0 seconds, consistent with the presence of Mesozoic clastic sedimentary rocks (possibly containing interbedded basalt flows) beneath the Jurassic basalt, as encountered in CC#3. There is no strong basal reflection on the northwestern half of the profile that would indicate a contact between the Mesozoic sequence and crystalline basement rock. The position of the label "B" in Figure 2.4, at 0.9 seconds, is meant to indicate where the amplitude of the

reflected energy from the layered Mesozoic sequence is clearly above the noise. The deepest visible reflections on VT-3b do not define the base of the Mesozoic sequence. What at first glance appears to be a possible candidate for a dipping contact between sedimentary rock and crystalline basement on the southeastern half of the profile (at approximately 1.0 sec) is actually the fortuitous alignment of faulted, but essentially horizontal, units within the Mesozoic sequence.

In what follows, we will refer to the entire package of reflections beneath the "J" as "B". Unlike previous investigators, we interpret those reflections as due to lithologic contrasts within a faulted package of essentially horizontal Mesozoic sedimentary and volcanic rocks.

Vertical Offsets of the Mesozoic Units

We begin by discussing features within the "B" units, proceeding along the profile from northwest to southeast.

CDP points 0 - 200

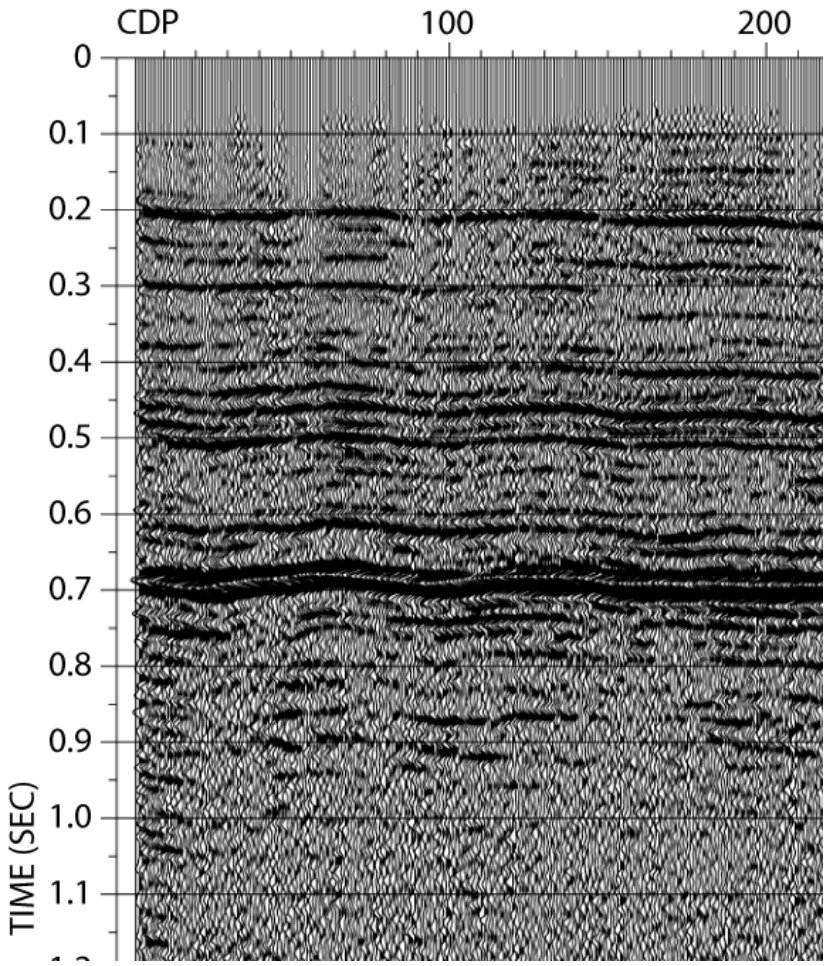

Figure 2.5 Northwestern end of VT-3b, between CDP 0 and 200.

Between CDP 0 and 200, on the northwestern end of VT-3b, the reflectors above the "J" horizon at 0.7 seconds are almost continuous (Figure 2.5). The "B" units beneath the "J" have much the same appearance. There are no obvious offsets of reflectors, although there is apparent up-warping near CDP 60 and 120. This warping appears to affect the entire section. We note in particular an absence of dip on the "B" reflections.

CDP points 190 - 450

Figure 2.6 shows the central section of VT-3b, between CDP 190 and 450. The character of the profile between CDP 190 and the bend in the line at CDP 300 is similar to that further to the northwest. The "J" reflector at 0.7 seconds is strong, and the underlying Mesozoic reflectors are essentially horizontal and continuous. There appears to be a minor disruption of the "B" package at CDP 230 and 0.8 seconds: overlying reflectors do not appear to be involved, and this may be an artifact of the data collection or processing.

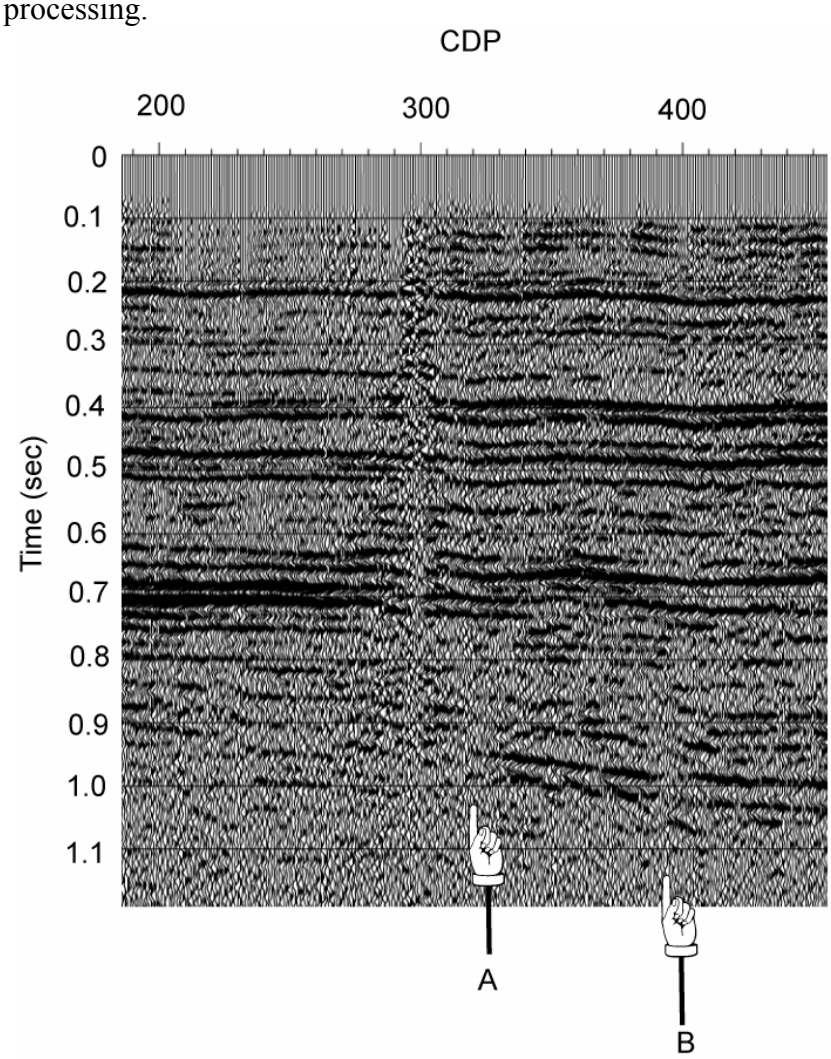

Figure 2.6 Central part of seismic reflection profile VT-3b. The symbols point to near-vertical faults A and B, with down-to-the-east displacement within the Mesozoic section.

The geometry of the profile undergoes a minor kink or bend in the vicinity of CDP 300 where the line layout on State Route 165 (Old Trolley Road), forming the northwestern half of the profile, was transferred onto State Route 642 (Dorchester Road) for the remainder of the survey. The intersection of these roads, and the ensuing bend in VT-3b recording geometry, is near Old Dorchester State Park (labeled as Fort Dorchester Figure 2.2). This is an extremely important part of the profile, and our reprocessing took this bend into account. However, the non-linear recording geometry resulted in un-avoidable loss of coherence in the CDP gathers. This is apparent in Figure 2.6 as the narrow zone of low resolution in the profile, most evident between CDP 290 and 300.

The character of the "B" reflectors changes a short distance beyond the bend in the profile, at CDP 320. There is a sudden loss of horizontal continuity of the "B" reflections at that point, indicating the presence of a fault (fault A in figure 2.6). Another disruption of the "B" reflector continuity occurs further to the southeast along the line at CDP 390, indicating another fault (fault B in Figure 2.6). The deeper "B" reflectors between CDP 320 and 390 (at 0.95 - 1.05 seconds) show an apparent dip to the southeast, indicating that some down-to-the-east rotation of those units has occurred. In significant contrast, the B reflectors between CDP 390 and 450 (to the southeast of fault B) are almost horizontal, further evidence of relative movement of the "B" reflector section between the two faults.

The strong, simple "J" reflection also changes in the vicinity of the bend in the profile. A change in "J" was noted by previous workers on adjacent line SC-10 as well as SC-4, and was interpreted as a "zone of missing J" on the southeastern ends of those profiles (e.g., figure 1 of Hamilton et al., 1983). Figure 2.6 indicates that "J" is not missing on VT-3b. The reflector becomes weaker, more complex, and it deepens above the zone of down-to-the-east faulting of the underlying "B" reflectors. This change in "J" may first occur near CDP 280 where the reflection appears to be truncated and slightly offset down-to-the-east: a change in reflection character is clearly apparent by CDP 320, where the temporal width of the reflection has substantially increased. Unfortunately, the image in the CDP range 280-320 is degraded by the bend in the line and lacks the resolution necessary to determine unequivocally whether or not the "J" and immediately adjacent reflections are offset by the faulting affecting the deeper "B" reflectors (fault A in Figure 2.6). The resolution of the data in that regard is not an issue for the remaining, southeastern, section of VT-3b.

CDP 400 - 600: Faulting of the Mesozoic-Cenozoic Section

Figure 2.7 shows the southeastern end of VT-3b, between CDP 400 and 600. The "B" reflections are offset by major down-to-the-east faulting at approximately CDP 520 (indicated by C in Figure 2.7). Cross-correlation of the "B" reflections in the time interval 0.85 - 1.05 seconds between CDP 410 and 470, with their counterparts between CDP 530 and 560 indicates that those horizons are offset by 0.080 seconds. This translates to approximately 200 meters of vertical displacement, assuming a velocity of 5.0 km/sec for the Mesozoic clastic sedimentary rocks.

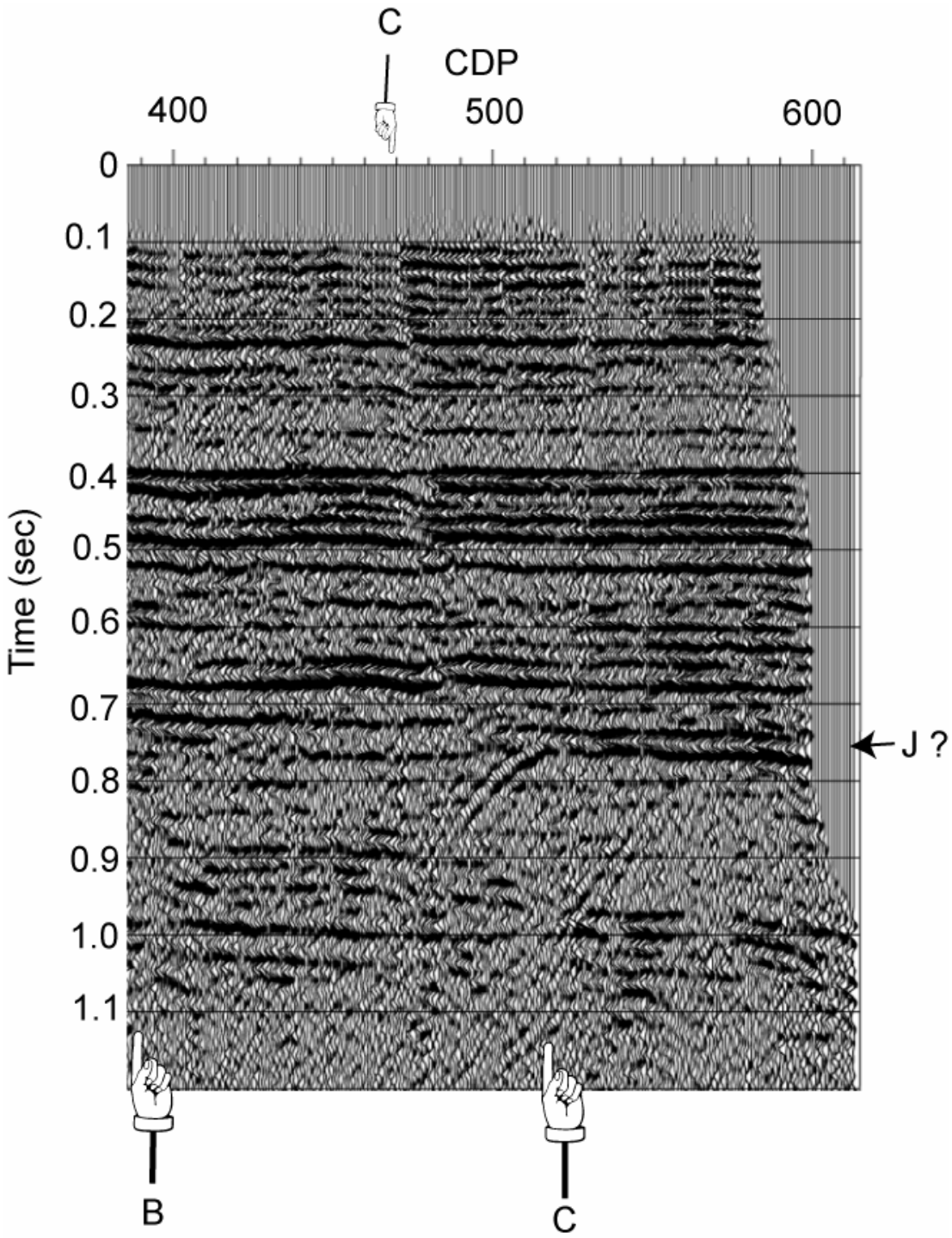

Figure 2.7 The southeastern end of seismic reflection profile VT-3b. The symbols point to near-vertical faults with down-to-the-east displacement within the Mesozoic section. Reverse offset of the shallowest resolved Tertiary sediments by fault C at CDP 470 is pointed out at the top of the figure. The interpreted reflection from the "J" horizon (top of Jurassic basalt) is indicated. Note the abundance of diffracted energy in the vicinity of fault C.

The entire Mesozoic and Tertiary section is offset by fault C between CDP 470 and CDP 520. Reverse offset is clearly evident in the shallowest sediments between 0.1 and 0.3 seconds, and in the "K" package between 0.4 and 0.5 seconds. The inferred location of the "J" horizon on the southeastern end of the profile is at 0.75 seconds. The inferred Jurassic reflector is truncated by the faulting at CDP 500 but, in contrast to the overlying Upper Cretaceous sediments, it exhibits minor normal (down-to-the east) displacement. The two-way time of 0.7 seconds in Figure 2.7 marks the transition from normal to reverse displacement of the reflectors.

The temporal offsets are similar on all the Tertiary and Cretaceous sedimentary units, and are near the limit of resolution of our data. We observe 6 to 10 msec of temporal offset on reflections at less than 0.3 seconds two-way time. Assuming a velocity of 2.0 km/sec, this translates to 6 to 10 meters of vertical displacement.

Intense diffracted energy is a characteristic feature of fault C on line VT-3b. This was first observed on individual shot gathers, and led to our reprocessing of line VT-3b. Inspection of Figure 2.7 shows that the tops of the diffraction hyperbolae (and hence, the sources of the scattering) are not always at the location of the fault plane indicated by offset and truncated reflectors (see also Figure 2.4). For example, there is a prominent diffraction apex at 0.8 seconds near CDP 560 in Figure 2.7. This indicates that fault C is not the only fault present in the "B" units near the southeastern end of line VT-3b. It is the most significant imaged fault, but concentration of the diffracted energy suggests that others are nearby.

Fault Strike, Spatial Extent and Conclusions

The location of fault C is indicated on Figure 2.2, by the red star on line VT-3b. We have scrutinized our hardcopies of the CMP stacks from all the SC lines shown in Figure 2.2, as well as all the Virginia Tech Regional Geophysics Lab reflection profiles. Line SC-10, located across the Ashley River from line VT-3b, shows the features resolved on the southeastern half of VT-3b. Strong diffractions and disruption of the "B" units are evident on the SC-10 stacked section. Unfortunately, the resolution of the SC data is very poor. Figure 2.2 shows the location of those features on SC-10, as a star plotted on that line. Line SC-4 is approximately 15 km to the south of VT-3b. We observe a very strong diffraction pattern originating within the B units near the end of that profile. That feature on SC-4 is similar to the diffraction pattern associated with fault C imaged on line VT-3b: a star in Figure 2.2 marks the location of the inferred fault edge diffractions on line SC-4. The original CMP stack of seismic profile VT-5, which trends approximately north-south, and is located north of Summerville (Figure 2.2) shows evidence of faulting of the "B" sequence, "J" reflector and very significant deformation of the overlying sedimentary units. These features were interpreted by Costain and Coruh (1989) as associated with a buried Triassic basin (Jedburg basin): the location is indicated on Figure 2.2 by a star on line VT-5. Seismic line SC-6 to the northeast of Summerville (Figure 2.2) shows equivocal evidence for faulting of the B units: the location is indicated by a star in Figure 2.2.

We propose that the stars shown in Figure 2.2 demarcate an active fault zone. The likelihood that faults A, B and C shown in figures 2.4, 2.6 and 2.7 are inactive and had nothing to do with the 1886 shock is exceedingly remote. Figure 2.2 shows that the

imaged faults A, B and C are directly above the hypocenters of the largest earthquakes in the northerly trending belt of events defining the Middleton Place - Summerville seismic zone. The evidence points to the existence of a north-striking zone of reactivated, high-angle Mesozoic extensional faulting extending from somewhere south of Rantowles, through the imaged faults on line VT-3b and northward past Summerville to intersect line VT-5 and possibly SC-6. We think it likely that the 1886 mainshock and major aftershocks involved pure strike-slip rupture along most of this zone. This faulting may have ruptured and otherwise deformed the ground surface in numerous locations. Some of the descriptions of railroad track distortion by Dutton (1889) may reflect co-seismic strain and not necessarily geotechnical failure of the ground due to shaking.

Additional insight into this problem will require a long-term commitment to earthquake monitoring in the Summerville area to continue collection of hypocenter and focal mechanism data of sufficient accuracy for geological interpretation. High resolution seismic reflection imaging of the shallow subsurface (upper 200 meters) in the vicinity of fault C on line VT-3b must be undertaken to establish whether or not this fault exhibits Quaternary offset. All available seismic reflection data in the area should be reprocessed using modern techniques and re-interpreted in light of this study.

Acknowledgments

This report builds upon the foundation of scientific investigation established by Dr. John Costain and Dr. Cahit Coruh, former directors of the Virginia Tech Regional Geophysics Laboratory, and now retired from the Department of Geosciences at Virginia Tech. We used data processing software made available by Landmark Graphics Corporation via the Landmark University Grant Program.

References
Part 2

Behrendt, J.C., R.M. Hamilton, H.D. Ackermann and V.J. Henry (1981). Cenozoic faulting in the vicinity of the Charleston, South Carolina, 1886 earthquake, Geology, 9, 117-122.

Coruh, C., J.K. Costain, J.K. Behrendt, and R.M. Hamilton (1981). New reflection seismic evidence for deformation of Mesozoic sediments near Charleston, S.C., Geol. Soc. Am., Abstracts with programs, 13,431.

Costain, J.K. and C. Coruh (1989). Tectonic setting of Triassic half-grabens in the Appalachians: Seismic data acquisition, processing and results, *in* Extensional Tectonics and Stratigraphy of the North Atlantic Margins, Tankard, A.J. and H.R. Balkwill, eds., AAPG Memoir 46, 155-174.

Dutton, C.E. (1889). The Charleston Earthquake of August 31, 1886, U.S. Geological Survey Ninth Annual Report 1887-88, p. 203-528.

Gohn, G.S. (1983). Geology of the basement rocks near Charleston, South Carolina - Data from detrital rock fragments in Lower Mesozoic(?) rocks in Clubhouse Crossroads test hole #3, *in* Gohn, G.S., ed., Studies Related to the Charleston, South Carolina, Earthquake of 1886--Tectonics and Seismicity, U.S. Geological Survey Professional Paper 1313, E1-E22.

Hamilton, R.M., J.C. Behrendt and H.D. Ackermann (1983). Land Multichannel Seismic-Reflection Evidence for Tectonic Features Near Charleston, South Carolina, *in* Gohn, G.S., ed., Studies Related to the Charleston, South Carolina, Earthquake of 1886--Tectonics and Seismicity, U.S. Geological Survey Professional Paper 1313, I1-I18.

Lanphere, M.A. (1983). $^{40}Ar/^{30}Ar$ ages of basalt from Clubhouse Crossroads test hole #2, near Charleston, South Carolina, *in* Gohn, G.S., ed., Studies Related to the Charleston, South Carolina, Earthquake of 1886--Tectonics and Seismicity, U.S. Geological Survey Professional Paper 1313, B1-B8.

Schilt, F.S., L.D. Brown, J.E. Oliver and S. Coffmann (1983). Subsurface structure near Charleston, South Carolina; Results of COCORP reflection profiling in the Atlantic Coastal Plain, *in* Gohn, G.S., ed., Studies Related to the Charleston, South Carolina, Earthquake of 1886--Tectonics and Seismicity, U.S. Geological Survey Professional Paper 1313, H1-H19.

Yantis, B.R., J.K. Costain and H.D. Ackermann (1983). A reflection seismic study near Charleston, South Carolina, *in* Gohn, G.S., ed., Studies Related to the Charleston, South Carolina, Earthquake of 1886--Tectonics and Seismicity, U.S. Geological Survey Professional Paper 1313, G1-G20.